Enhancing the removal of organic micropollutants by nanofiltration membrane with Fe (III)–tannic acid interlayer: Mechanisms and environmental implications

Wenyu Liu [a], Li Long [a], Zhe Yang [a], Li Wang [a], Qimao Gan [a], Shenghua Zhou [a], Pulak Sarkar [a], Hao Guo [b,*], Chuyang Y. Tang [a,*]

[a] Department of Civil Engineering, The University of Hong Kong, Pokfulam, Hong Kong SAR, China

[b] Institute of Environment and Ecology, Tsinghua Shenzhen International Graduate School, Tsinghua University, Shenzhen 518055, China

* Corresponding authors

Hao Guo (ORCID: 0000-0002-0688-5431)

Tel: +86 15889350923

E-mail: guohao@sz.tsinghua.edu.cn

Chuyang Y. Tang (ORCID: 0000-0002-7932-6462)

Tel: +852 2859 1976

E-mail: tangc@hku.hk

Abstract

Nanofiltration technology has been applied in a variety of water treatment scenarios. However, conventional thin-film composite (TFC) membranes fail to remove emerging organic micropollutants (OMPs) efficiently. Here we applied thin-film nanocomposite membrane with an interlayer (TFNi) of Fe (III)-tannic acid to remove various types of OMPs, such as endocrine disrupting chemicals (EDCs), pharmaceutically active compounds (PhACs), and perfluoroalkyl substances (PFASs). Compared to the pristine TFC membrane, TFNi membrane exhibited crumpled morphology and its rejection layer was denser, better cross-linked and possessed smaller average pore size with narrower distribution. Significant enhancement in water-OMPs selectivity of PhACs and PFASs was observed. The mechanism lies in the effects of interlayer in improving the membrane permeance to water and meanwhile reducing the permeance to some OMPs by enhancing size exclusion effects. This work confirms the effectiveness of using TFNi membrane to simultaneously enhance the OMPs rejection and water permeance. The unraveled mechanism might inspire the future development of high-performance nanofiltration membranes targeting OMPs removal.

Keywords

Organic micropollutants; Nanofiltration membranes; Interlayer; Fe (III)–tannic acid

1. Introduction

The widespread emergence of organic micropollutants (OMPs) in aquatic environment, such as endocrine disrupting chemicals (EDCs), pharmaceutically active compounds (PhACs), and poly- or perfluoroalkyl substances (PFASs), has posed a great menace to water safety (Houtz et al., 2013; Lapworth et al., 2012; Petrie et al., 2015; Schwarzenbach et al., 2006; Tran et al., 2018). Although these OMPs are commonly present at low concentration (e.g., ng/L–μg/L), their ecotoxicological effects can be of high concern (Fent et al., 2006; Williams et al., 2003). It has been reported that some EDCs, PhACs, and PFASs at environmental concentration could impact the reproduction, development, and locomotion of aquatic organisms (Krafft and Riess, 2015; Schmidt et al., 2011; Souza et al., 2013). Such toxic and bioaccumulating compounds might exert adverse chronic effects on human health through multiple exposure routes including direct skin contact and uptake of contaminated water or food (Barbosa et al., 2016; Ben et al., 2018; Luo et al., 2014). Therefore, it is imperative to effectively remove OMPs from water.

Nanofiltration (NF) technology has been extensively applied in water treatment scenarios such as drinking water purification and water reclamation (Fane et al., 2011; Guo et al., 2021a; Shannon et al., 2008; Tang et al., 2018). The most widely used NF membranes are thin-film composite (TFC) membranes that consist of a dense polyamide layer on the top of a porous polymer substrate (Lau et al., 2012; Warsinger et al., 2018). Although TFC membranes often exhibit robust rejection of many solutes including divalent salts (Warsinger et al., 2018), the removal efficiency of some OMPs, especially those with relatively small molecular size, could be lower than 50% due to weak size exclusion effects (Guo et al., 2019; Jin et al., 2010; Miyashita et al., 2009; Van der Bruggen and Vandecasteele, 2002; Zhao et al., 2021). Moreover, the rejection

of some hydrophobic/polar OMPs (e.g., EDCs, nitrosodimethylamine) might be further jeopardized by the unfavorable solute-membrane hydrophobic/polar interactions (Nghiem et al., 2004, 2005; Schäfer et al., 2011; Steinle-Darling et al., 2007; Verliefde et al., 2009). Such insufficient removal of concerned OMPs would significantly lower the quality of product water.

To enhance the membrane rejection of OMPs, it is essential to improve the membrane selectivity of water/OMPs, which is often indicated by the ratio of membrane permeance to water (A) over that to OMPs (B_{OMP}) (Guo et al., 2022). Increasing the A value and/or reducing the B_{OMP} value could benefit the membrane selectivity. For instance, an effective approach to increase the membrane water/OMPs selectivity is to introduce a highly selective coating layer on its surface to reduce the OMPs permeance (Ben-David et al., 2010; Huang et al., 2021; Kim et al., 2008). However, this strategy often suffers the decreased water permeance, which might result in higher energy consumption (Guo et al., 2016; Guo et al., 2017a; Yang et al., 2019a). Similarly, thin film nanocomposite (TFN) membranes also show limited enhancement of water/OMPs selectivity due to the agglomeration of nanofillers (Dai et al., 2019; Lau et al., 2015; Yang et al., 2020a; Zhao et al., 2019).

In recent years, a novel type of thin-film nanocomposite membranes with interlayered structure (TFNi) has been reported to exhibit significantly enhanced water permeance and rejection of solutes compared to conventional TFC membranes (Gao et al., 2019; Karan et al., 2015; Sarango et al., 2018; Yang et al., 2020a; Yuan et al., 2019). The interlayer, often made of nanoparticles (e.g., Ag nanoparticles, carbon nanotubes, metal-organic frameworks, covalent organic frameworks) or interfacial coating materials (e.g., polydopamine, iron-tannic acid), could optimize the water transport pathways and facilitate better formation of polyamide layer (Li et al., 2015; Long et al.,

2022; Sarango et al., 2018; Yang et al., 2019b; Yang et al., 2020b; Yang et al., 2018; Yuan et al., 2019). However, most of the research merely focused on water permeance and salt rejection. There lacks an in-depth study of applying TFNi membranes to remove various types of OMPs, which is a critical issue for the membrane-based water treatment technology. Although it is reasonable to expect a better water/OMPs selectivity considering the proven effects of interlayer in enhancing the membrane water/salt selectivity, the specific role of interlayer in affecting the removal of OMPs still needs systematic investigation.

In this study, we used iron-tannic acid, a highly selective material to OMPs (Guo et al., 2019), as an interlayer of the TFNi membrane. The membrane properties such as morphology, structures, chemical composition, surface charge, contact angle, and pore size distribution were characterized. We also evaluated the membrane separation performance including water permeance and rejection of salt, neutral molecules, and OMPs (i.e., EDCs, PhACs, and PFASs). The major objectives are (1) to investigate the effectiveness of TFNi membranes in the removal of OMPs of varied characteristics (e.g., size, hydrophobicity, charge) and (2) to understand how the interlayer tailors the membrane properties and thereby influences the interactions between OMPs and membranes. Our work may provide fundamental insights of designing high-performance NF membranes targeting OMPs removal.

2. Materials and methods

2.1. Materials and chemicals

In this work, chemicals were of analytical grade unless specific description. All water-based solution was prepared with Milli-Q water. Polysulfone (PSf, pellets, MW~35,000), N,N-dimethylformamide (DMF), piperazine (PIP), trimesoyl chloride (TMC) were purchased from Sigma-Aldrich. These chemicals, together with n-hexane (HPLC grade, 95%, RCI Labscan), iron (III) chloride anhydrous ($FeCl_3$, Dieckmann), tannic acid (TA, Macklin), tris (hydroxymethyl) aminomethane (Tris, Acros), hydrochloric acid (HCl, 37 wt%, VWR) were used to fabricate membranes. Sodium sulfate anhydrous (Na_2SO_4) and sodium chloride (NaCl) were purchased from Dieckmann. Potassium chloride (KCl, 99.99%, Aladdin) was used to prepare background electrolyte in zeta potential measurement. Neutral molecular probes (**Table 1**) used to determine membrane pore size were glycerol (Dieckmann), D-glucose (Uni-Chem), D-(+)-sucrose (Dieckmann), D-(+)-raffinose pentahydrate (Sigma-Aldrich), and dextran (D-Chem). OMPs investigated in this work included four EDCs, four PhACs, and five PFASs (**Table 1**). Methylparaben (MP), ethylparaben (EP), propylparaben (PP), benzylparaben (BP), sulfadiazine (SDZ), sulfamethoxazole (SMX), sulfamethazine (SMZ), and trimethoprim (TMP) were purchased from Sigma-Aldrich. PFASs were perfluorobutyric acid (PFBA, Alfa Aesar), potassium nonafluoro-1-butanesulfonate (PFBS potassium salt, TCI), perfluoro (2-methyl-3-oxahexanoic) acid (Genx, Macklin), sodium perfluorooctanoate (PFOA sodium salt, Alfa Aesar), potassium perfluorooctanesulfonate (PFOS potassium salt, Sigma-Aldrich). Methanol (VWR) was used to prepare 1 g/L OMPs stock solution. Methanol (Optima LC/MS, Fisher Chemical), acetonitrile (Optima LC/MS, Fisher Chemical), formic acid (MS grade, Waters), and ammonium acetate (TCI) were used to prepare LC-MS/MS mobile phase.

2.2. Membrane fabrication

The pristine substrate was synthesized via phase inversion method with a cast solution of 15 wt% PSf in DMF following our previous work (Ma et al., 2017). To coat interlayer onto PSf substrate, 1.2 g/L $FeCl_3$ solution was firstly poured onto substrate and then dumped after 3 min. Droplets attached on the substrate surface were rolled off by a PTFE roller. 4 g/L tannic acid (dissolved in Tris, pH 8.5 adjusted by HCl) was subsequently poured onto substrate, reacting for 1 min before rinsed several times with deionized water. To fabricate the TFNi membrane, the modified substrate was firstly immersed in PIP solution (0.2 wt% in water) for 3 min. After removing extra PIP with PTFE roller, the membrane was immediately soaked in TMC (0.1 wt% in hexane) to conduct interfacial polymerization (IP) reaction. After reacting for 1 min, the membrane was thoroughly rinsed with hexane and heat-cured in 60 ℃ oven for 5 min. The TFC membrane was fabricated in the same procedures of IP with pristine PSf substrate.

2.3. Membrane characterization

The microscopic morphology of membrane surface was characterized by a field emission scanning electron microscope (FE-SEM, S-4800, Hitachi, Japan) with an accelerating voltage of 5 kV. The cross-sectional images were obtained from a transmission electron microscope (STEM, Talos F200X, Thermo Scientific) at an accelerating voltage of 200 kV. The element composition of membrane cross-section was examined by energy-dispersive X-ray spectroscopy (EDX) equipped in the STEM. The membrane surface roughness was measured by atomic force microscope (AFM, Dimension Icon, Bruker, Germany) and the data were processed by using software Gwyddion. Element composition of the membrane top surface was determined by using an X-ray photoelectron spectrometer (XPS, K-Alpha, Thermo Scientific). The survey spectra were acquired at a pass energy of 150 eV and energy step size of 1 eV. For high-

resolution spectra, the pass energy and energy step size were 50 eV and 0.1 eV, respectively. Software Avantage was used to process XPS data. The membrane functional groups were analyzed by using attenuated total reflection Fourier transform infrared (ATR-FTIR) spectroscopy (Nicolet iS5 FTIR Spectrometer with iD5 ATR Accessory, Thermo Scientific). The water contact angle was measured by using an optical tensiometer (Attension Theta, Biolin Scientific, Sweden). The zeta potential of membrane surface was measured by an electrokinetic analyzer (SurPASS 3, Anton Paar, Austria) over a pH range from 3 to 10 with 1 mM KCl as background electrolyte. The solution temperature was kept at 25 ℃ and pH was adjusted by adding HCl or KOH.

2.4. Filtration experiments

The filtration experiments were performed in a bench-scale cross-flow filtration setup (**Fig. S1**). Feed solution (25 ℃, pH 6.5–7.5) was composed of 1 g/L Na_2SO_4 for salt filtration experiments and 200 mg/L single neutral solute for the neutral molecule filtration tests. Membranes were pre-compacted at 5 bar with a crossflow velocity of 16.7 cm/s for two hours before sample collection. The conductivity proportional to salt concentration was measured by a portable water tester (Ultrameter II 6PFC^{E}, Myron L). A total organic carbon (TOC) analyzer (TOC-$L_{CPH/CPN}$, Shimadzu, Japan) was used to quantify the concentration of neutral molecules. All the experiments were repeated at least three times. Water flux J_V ((L m^{-2} h^{-1}), water permeance A (L m^{-2} h^{-1} bar^{-1}), solute rejection R (%), and solute permeance B (L m^{-2} h^{-1}) were calculated as below:

$$J_V=\frac{\Delta m}{S\times\Delta t\times\rho} \quad (1)$$

$$A=\frac{J_V}{\Delta p-\Delta\pi} \quad (2)$$

$$R=(1-\frac{C_p}{C_f})\times 100\% \quad (3)$$

$$B=(\frac{1}{R}-1)\times J_V \quad (4)$$

where Δm (kg) is the amount of permeate collected during a period of Δt (h), S (m^2) is the effective filtration area, ρ (kg L^{-1}) is the density of water, Δp (bar) is the applied pressure, $\Delta\pi$ (bar) is the osmotic pressure across membrane, C_f and C_p refer to the solute concentration of feed and permeate, respectively.

2.5. OMPs analysis method

A cocktail of all OMPs with each compound at a concentration of 200 μg/L was used for OMPs rejection tests. 600 mg/L NaCl was added to simulate the typical ionic strength relevant to water reuse. The feed solution was kept at 25 ℃, pH 6.5–7.5. Membranes were compacted at 5 bar with a crossflow velocity of 16.7 cm/s for six hours in the presence of OMPs to reach stable rejection performance (**Fig. S2**) before sample collection. The concentration of OMPs was analyzed by using liquid chromatography with tandem mass spectrometry (LC-MS/MS, 1290 Infinity, Agilent; 3200 QTRAP, AB SCIEX, Singapore). The reversed-phase column (ZORBAX Eclipse Plus C18, Agilent) was 2.1×50 mm in dimension with particle size of 1.8 μm. Detailed LC-MS/MS settings can be found in our previous work (Guo et al., 2017b; Guo et al., 2021b). OMPs rejection (R), and OMPs permeance (B) were calculated according to **Eqs. (3)** and **(4)**.

Table 1

Physicochemical properties of organic micropollutants and molecular probes.

Classification	Compound	Formula	Molecular weight (Da)	Stokes radius[a] (nm)	pK_a [b]	Log K_{ow} [b]
Hydrophobic endocrine-disrupting chemicals (EDCs)	Methylparaben (MP)	$C_8H_8O_3$	152.2	0.300	8.4	2.0
	Ethylparaben (EP)	$C_9H_{10}O_3$	166.2	0.326	8.3	2.4
	Propylparaben (PP)	$C_{10}H_{12}O_3$	180.2	0.351	8.2	2.9
	Benzylparaben (BP)	$C_{14}H_{12}O_3$	228.2	0.395	8.2	3.6
Hydrophilic pharmaceutically active compounds (PhACs)	Sulfadiazine (SDZ)	$C_{10}H_{10}N_4O_2S$	250.3	0.398	6.4	-0.1
	Sulfamethoxazole (SMX)	$C_{10}H_{11}N_3O_3S$	253.3	0.376	1.6, 5.7	0.9
	Sulfamethazine (SMZ)	$C_{12}H_{14}N_4O_2S$	278.3	0.439	2.6, 7.6	0.1
	Trimethoprim (TMP)	$C_{14}H_{18}N_4O_3$	290.3	0.466	3.2, 6.8	0.9
Negatively charged perfluoroalkyl substances (PFASs)	Perfluorobutyric acid (PFBA)	$C_4HF_7O_2$	214.0	0.280	0.4	2.2
	Perfluorobutane sulfonic acid (PFBS)	$C_4HF_9O_3S$	300.1	0.337	0.1	2.3
	Perfluoro (2-methyl-3-oxahexanoic) acid (Genx)	$C_6HF_{11}O_3$	330.0	0.359	2.8	3.6
	Perfluorooctanoic acid (PFOA)	$C_8HF_{15}O_2$	414.1	0.415	1.3	1.6
	Perfluorooctane sulfonic acid (PFOS)	$C_8HF_{17}O_3S$	500.1	0.460	0.1	3.1
Neutral hydrophilic molecules	Glycerol	$C_3H_8O_3$	92.1	0.224	14.4	-1.8
	Glucose	$C_6H_{12}O_6$	180.1	0.323	12.9	-2.6
	Sucrose	$C_{12}H_{22}O_{11}$	342.3	0.478	Solution is neutral to litmus	-3.7
	Raffinose	$C_{18}H_{32}O_{16}$	504.0	0.585		-5.1
	Dextran	$C_{36}H_{62}O_{31}$	990.9	0.752		-13.0

[a] Stokes radius was calculated by using Wilke-Chang equation and Stokes-Einstein equation (Deen, 1987).

[b] The dissociation constant (K_a) and octanol-water partitioning coefficient (K_{ow}) were obtained from references (Guo et al., 2019; Guo et al., 2021b; Huang et al., 2021; Steinle-Darling and Reinhard, 2008; Wang et al., 2015) and U.S. National Library of Medicine (https://pubchem.ncbi.nlm.nih.gov/). The pK_a indicates charge characteristics and log K_{ow} suggests hydrophobicity.

3. Results and discussion

3.1. Characterization results

The membrane microscopic morphology is shown in **Fig. 1**. the TFC membrane exhibited nodular surface morphology, which is typical for most PIP/TMC-based NF membranes. After introducing interlayer, the TFNi membrane presented strip-like morphology with surface roughness significantly increased from 9.7 ± 0.6 nm to 26.1 ± 0.2 nm. This might be induced by the change of substrate physicochemical properties—the Fe/TA coated substrates possessed smaller pore size (**Fig. S3**), increased surface roughness (**Fig. S3**), and improved hydrophilicity (**Fig. S4a**), which may alter the interfacial polymerization conditions and thereby affect the morphology of polyamide layer (Yang et al., 2020a; Yuan et al., 2020; Zhai et al., 2018).

Apart from morphology difference, the microscopic structure also varied between TFC and TFNi membranes. **Fig. 2** shows the TFNi membrane possessed distinct layered structure—a crumpled polyamide layer with thickness of 20 ± 5 nm on the top (**Fig. 2a-c**), an interlayer continuously spreading in the middle (**Fig. 2d**), and a porous polysulfone substrate at the bottom (**Fig. 2e**). In contrast, the STEM-EDX image of TFC membrane was less distinct (**Fig. S5**), and the color of polyamide layer appeared lighter in the STEM images (**Fig. S6**). These observations indicate the TFC membrane is probably looser than TFNi membrane (Tang et al., 2007a; Zhou et al., 2022), which is also confirmed by ATR-FTIR and XPS deconvolution results that will be presented in the next sub-section. In addition, we further notice that some nanovoids existed between the interlayer and polyamide film (**Fig. 2b**), which is likely to favor higher water permeance owing to self-guttering effect (Hu et al., 2023).

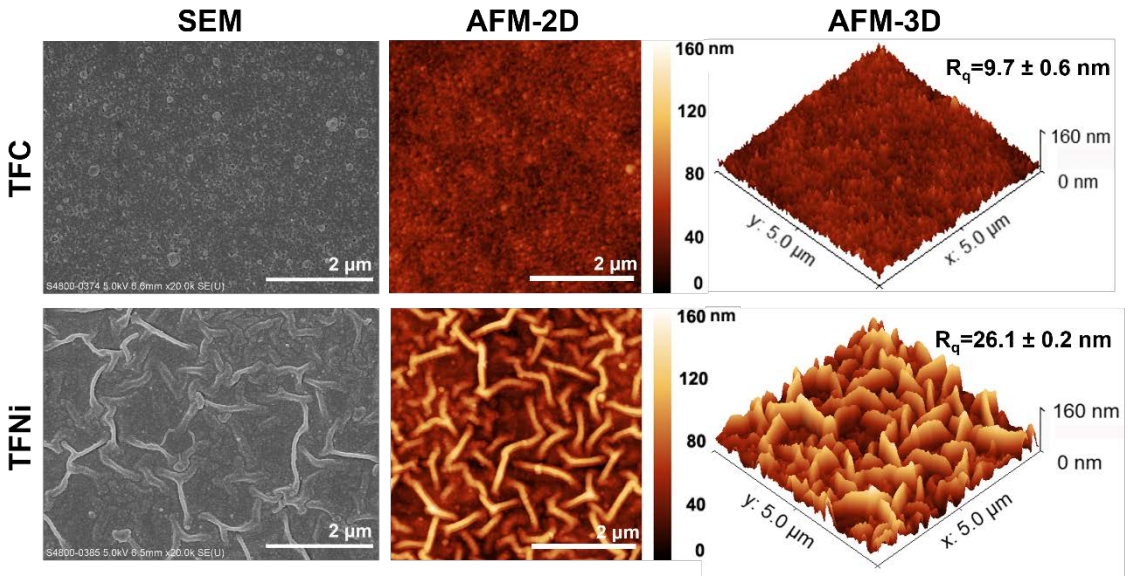

Fig. 1. SEM images, AFM-2D plane view, and AFM-3D view of the top surface for TFC and TFNi membranes. The roughness R_q value is the root mean square average of height deviations from the mean image data plane. Standard deviation was obtained from three independently scanned images.

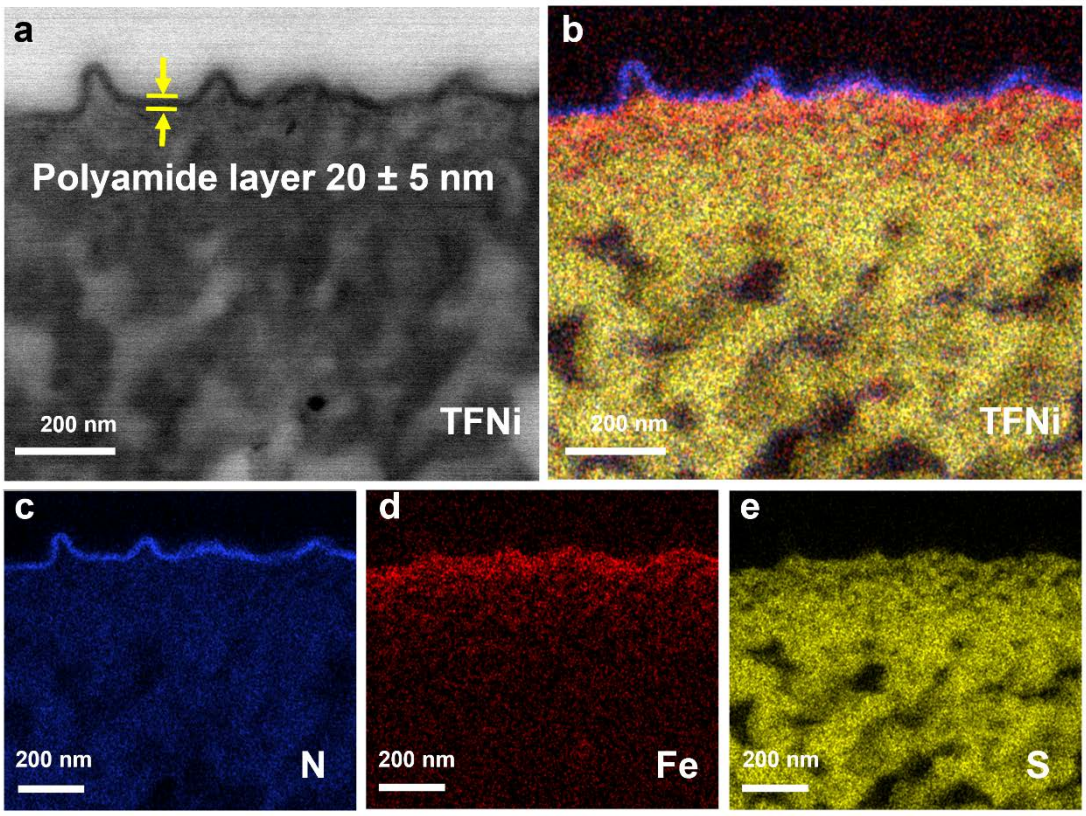

Fig. 2. (a) STEM cross-section image and (b) STEM-EDX elemental mapping of TFNi membrane with (c) element nitrogen (N, blue) as an indicator for polyamide layer, (d) iron (Fe, red) for interlayer, and (e) sulfur (S, yellow) for polysulfone substrate. Thickness of polyamide layer as denoted in yellow was measured by software Image J. Standard deviation was obtained by measuring at least ten positions.

The membrane chemical composition was characterized by ATR-FTIR and XPS. In ATR-FTIR spectra (**Fig. 3a**), the stretching vibration peaks of hydroxyl groups (~3400 cm^{-1}) and carbonyl groups (1716 cm^{-1}) (Heredia-Guerrero et al., 2014) appeared additionally in Fe/TA modified substrate compared to the pristine polysulfone substrate, confirming the successful coating of interlayer. The amide I band (~1615 cm^{-1}) (Tang et al., 2009) appeared more intense in the spectra of TFNi membrane than TFC membrane possibly due to a relatively higher density of polyamide. It is worthwhile note that the detection depth of FTIR ranges to several micrometers, thus the functional groups from substrate could be well detected, which may dilute the signal of amide I band especially when the polyamide layer is loose (Yang et al., 2022). Surprisingly, sulfur—a typical element from the substrate, was detected in TFC membrane by XPS of which the detection depth is normally less than 10 nm from the top surface (**Fig. 3b**). This potentially indicates the distribution of polyamide in TFC membrane was non-uniform, such that at some spots the polyamide might be too thin to cover the substrate completely, leading to the detection of sulfur from substrate. Moreover, the atomic ratio of oxygen over nitrogen (O/N) of TFNi membrane was smaller than TFC membrane, suggesting a higher cross-linking degree of polyamide in TFNi membrane, which is beneficial to improve separation performance.

In the high-resolution XPS spectra of C 1s (**Fig. 3c**), the normalized intensity of C=O deconvoluted peak of C1s at ~287.6 eV was higher in TFNi membrane compared to TFC membrane (see detailed data in **Table S1**). Since the detection depth of XPS is normally less than 10 nm (Tang et al., 2007b) which is much lower than the thickness of polyamide layer (**Table 2**), C=O is mainly attributed to the amide bond (O=C−N) or the hydrolysis product (O=C−O) of TMC that constitutes polyamide layer. Accordingly, a higher intensity of C=O potentially means higher content of polyamide on membrane

surface. This agrees well with previous STEM-EDX and ATR-FTIR results. The membrane surface charge for the TFC and TFNi membranes was negative and almost identical at pH~7 (**Fig. S4b**). This surface property affects the electrostatic repulsion toward the negatively charged PFASs as will be discussed in **Section 3.3**. Besides, the TFC membrane had a water contact angle of 59.4 ± 9.3° whereas that of TFNi membrane was 27.3 ± 3.9° (**Table 2**). Since the hydrophilic surface of the Fe/TA interlayer is completely blocked by the polyamide layer, such reduced contact angle might be partly related with the crumpled morphology of TFNi membrane.

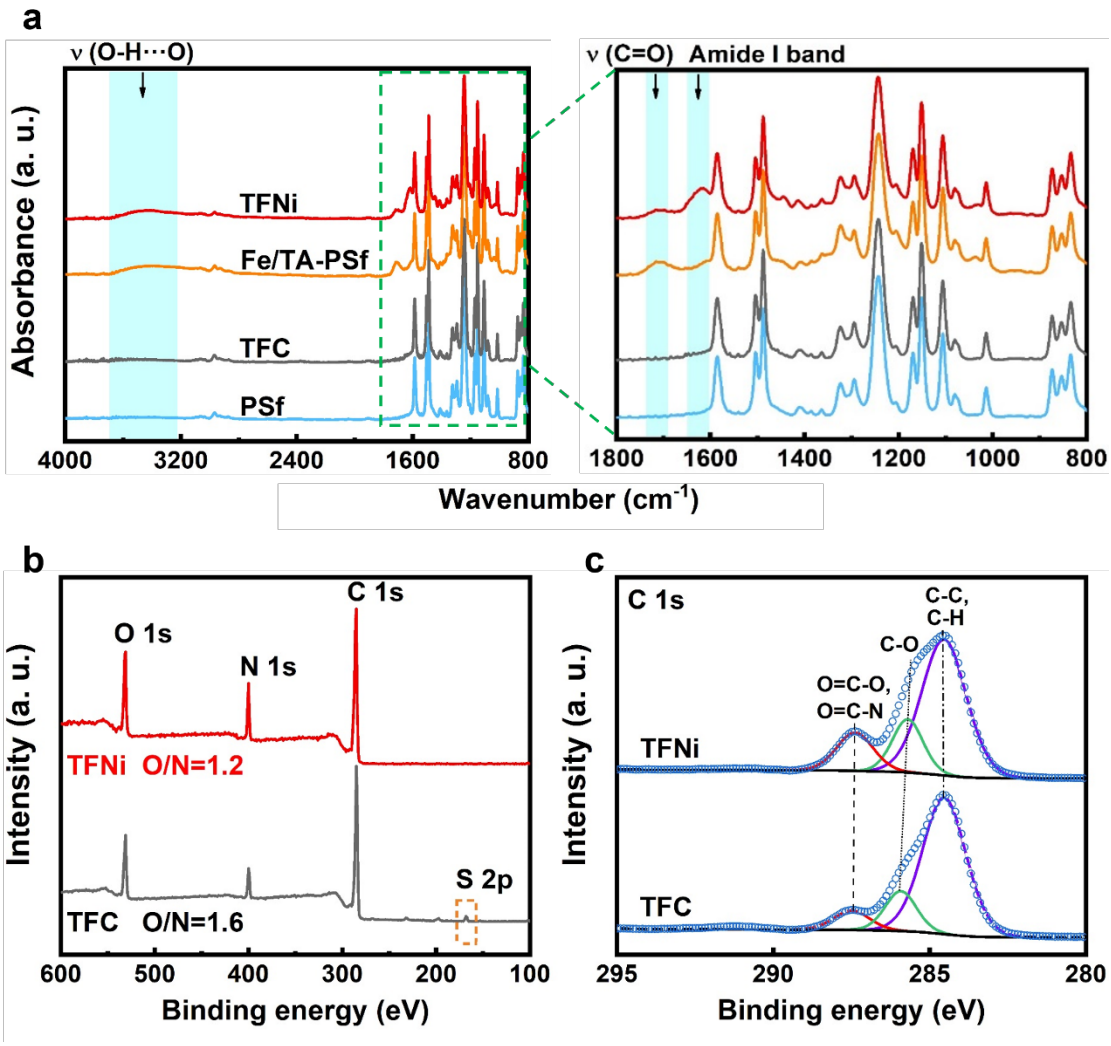

Fig. 3. (a) ATR-FTIR spectra of NF membranes and their substrates. Spectra differences are highlighted and annotated with peak type where ν stands for stretching vibration peaks. (b) XPS survey spectra of TFC and TFNi membranes. Element composition was

identified by software Avantage. The atomic ratio of oxygen over nitrogen (O/N) was obtained from high-resolution XPS scanning results of O 1s and N 1s. (c) High-resolution XPS spectra of C 1s with deconvoluted peaks. Peak assignment is annotated according to literature (Do et al., 2012; Tang et al., 2007b; Wilson and Langell, 2014). Peak percentage can be found in **Table S1**.

3.2. Separation performance

The TFNi membrane exhibited nearly tripled water permeance and significantly higher Na_2SO_4 rejection compared with the TFC membrane (**Table 2**). Such enhanced performance of TFNi membrane has been extensively documented in literature (**Table 3**), with a great deal of discussion about the effects of interlayer in optimizing water transport pathways and favoring better formation of polyamide rejection layer (Dai et al., 2020; Gao et al., 2019; Li et al., 2015; Yang et al., 2020b; Zhang et al., 2016). In this study, the increase of water permeance can be ascribed to (1) the gutter effect of interlayer that shortens lateral distance of water transport inside the less permeable polyamide layer (Long et al., 2022; Wang et al., 2022; Yang et al., 2020b), (2) self-guttering effect of nanovoids contained in TFNi membrane that optimizes water transport pathways (Hu et al., 2023), and (3) thinner and crumpled polyamide layer which may provide more effective filtration area with less resistance (Shao et al., 2022; Tan et al., 2018). Schematic illustrations of these effects are presented in **Table 3**. In the current study, the gutter effect plays a major role in enhancing water permeance (see details in **Supplementary materials S4**), which is consistent with existing modeling (Hu et al., 2023; Wang et al., 2022) and experimental studies (Long et al., 2022; Yang et al., 2020b).

In the filtration experiment of neutral hydrophilic molecules, we found the TFNi membrane displayed higher rejection (**Fig. 4**). Based on the rejection value, the membrane pore size can be determined with the assumption of log-normal distribution. The mean pore radius of TFNi membrane was estimated at 0.61 ± 0.03 nm whereas that of TFC membrane was 0.79 ± 0.08 nm, exhibiting a larger mean pore size with wider distribution (**Fig. 4**). As a result of such distinct pore size difference, the molecular weight cut-off (MWCO) of TFNi membrane was 270 Da, which was smaller than that

of TFC membrane (504 Da) (**Table 2**). Recalling the characterization results that show the TFNi membrane possessed a denser and better cross-linked polyamide layer, this separation performance toward neutral molecules further confirms the role of interlayer in tuning the pore size of polyamide layer, which may help enhance size exclusion effects in retaining OMPs (see OMPs rejection in **Section 3.3**).

Besides the enhanced separation performance as mentioned above, we also found the extent of such enhancement was dependent on the heat treatment time. Specifically, the water permeance and Na_2SO_4 rejection by TFC membrane decreased dramatically as the heat treatment prolonged whereas the separation performance of TFNi membranes remained almost the same (**Fig. S7a**). That is, the presence of interlayer has improved the membrane endurance to heat-curing process, making it more competitive to be applied in real production line where heat treatment is widely adopted. It is worthwhile to note that even under short heat curing time (i.e., 0 min or 2 min), some OMPs rejection was still enhanced by TFNi membrane (**Fig. S8**), indicating the role of interlayer in facilitating better formation of polyamide layer which will be discussed in **Section 3.3**. Furthermore, when the bare PSf substrate and Fe/TA-PSf substrate received heat treatment in 60 ℃ oven for designated time, the water permeance of PSf substrate dramatically decreased whereas that of the Fe/TA-PSf substrate was comparable to the original state (i.e., substrate without any heat treatment) (**Fig. S7b**). One possible explanation for these observations is that the substrate structure might be deformed during heat-curing process, which might greatly increase the water transport resistance from both the substrate and the polyamide layer due to pore shrinkage and severe funnel effect (Wang et al., 2022; Zhan et al., 2020a). However, the interlayer-coated substrate, endowed with rougher surface and smaller pore size (**Fig. S3**), might resist the potential structural deformation so that avoid introducing additional resistance

to water, thus maintaining the water permeance (see schematic illustration in **Table 3**).

Table 2

Membrane properties.

	Water permeance [a] ($L\ m^{-2}\ h^{-1}\ bar^{-1}$)	Na_2SO_4 rejection [a] (%)	MWCO [b] (Da)	Mean pore radius [b] (nm)	Thickness of polyamide layer [c] (nm)	Contact angle [d] (°)
TFC	7.4 ± 4.3	80.0 ± 11.4	504	0.79 ± 0.08	36 ± 10	59.4 ± 9.3
TFNi	18.8 ± 3.4	94.4 ± 3.5	270	0.61 ± 0.03	20 ± 5	27.3 ± 3.9

[a] Data were measured by using 1000 mg/L Na_2SO_4 as feed solution (25 °C, pH 7.0 ± 0.5) under the applied pressure of 5 bar at crossflow velocity of 16.7 cm/s. Experiments were repeated at least three times.

[b] The molecular weight cut-off (MWCO) was determined by the neutral solute of which the rejection was 90%. See estimation of pore size in **Supplementary materials S6**.

[c] Thickness of polyamide layer was measured from STEM image by software Image J at more than ten different positions (**Fig. S6**).

[d] Water contact angle was obtained from at least five independent measurements.

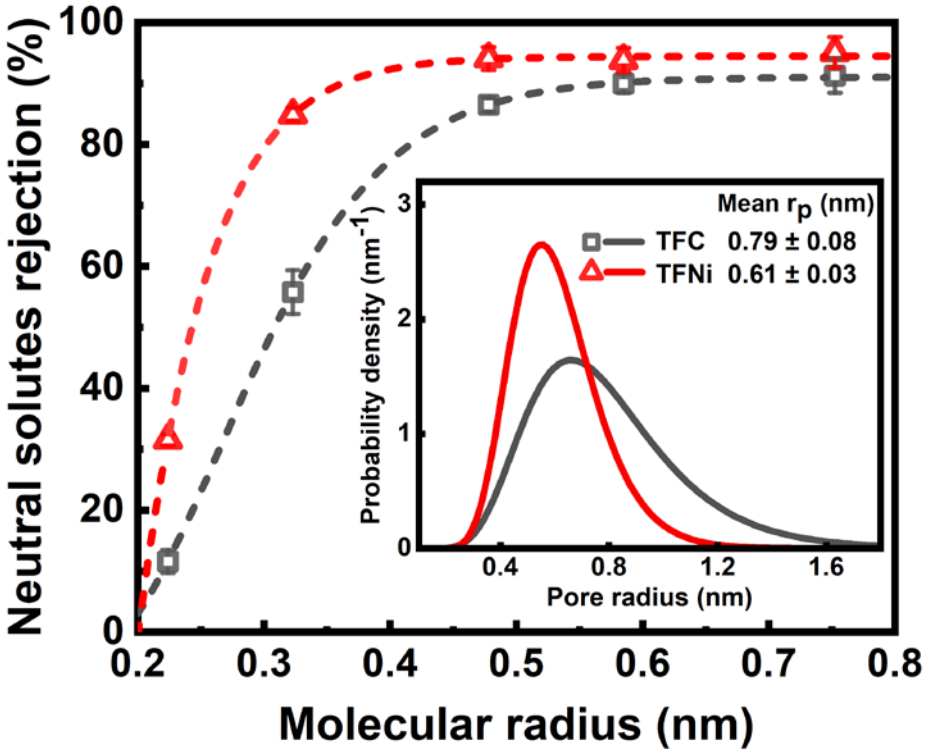

Fig. 4. Rejection of neutral solutes by TFC and TFNi membranes as a function of molecular radius. The solutes were glycerol, glucose, sucrose, raffinose, and dextran. The data points were obtained from at least three measurements. The dash lines were established assuming log-normal distribution of membrane pore size. Inset is the distribution of pore radius derived from the rejection results of neutral solutes. The mean pore radius and variance are also annotated. Pore size estimation method is described in **Supplementary materials S6**.

3.3. Rejection and selectivity of OMPs

Fig. 5a and **5b** present the rejection of OMPs by TFC and TFNi membranes as a function of Stokes radius of solutes. The dash line is established by fitting the rejection data of neutral molecular probes assuming log-normal distribution of membrane pore size. Since the removal of these neutral hydrophilic surrogates by NF membrane is governed by size exclusion (Bellona et al., 2004; Yang et al., 2017), here we term the fitted curve as the size-exclusion (SE) curve. Note that the SE curve of TFNi membrane was generally higher than TFC membrane as a result of smaller pore size (**Fig. 4**). Such enhanced size exclusion effects also partially account for the improved rejection of neutral hydrophilic PhACs and charged PFASs by TFNi membrane, as steric hindrance is confirmed to be one of the major factors influencing the rejection of these two types of OMPs by tight membranes (Nghiem et al., 2005; Tang et al., 2006; Wang et al., 2021). However, the rejection of OMPs can also affected by additional mechanisms such as charge interaction and hydrophobic interaction. Interesting results were found when we compared the removal trend of OMPs against neutral molecular probes. For TFC membrane, the rejection data of PFASs were scattered around the SE curve whereas other pollutants fell below the line (**Fig. 5a**). For TFNi membrane, the rejection data of PFASs were slightly above the SE curve whereas those of EDCs and some PhACs were lower (**Fig. 5b**). Such deviation from the SE curve implies there might exist multiple mechanisms influencing the retention of OMPs apart from size exclusion effects. For example, the hydrophobic interactions between solutes and membranes might account for the low rejection of EDCs. As shown in **Fig. S9**, the sorption amount of hydrophobic EDCs onto membranes was generally higher than other hydrophilic compounds probably due to hydrophobic interactions. Such high affinity to membrane would make it easier for EDCs to transport across membrane via convection and diffusion, resulting

in lower rejection (Guo et al., 2016; Nghiem and Schäfer, 2002). According to **Fig. S10**, the sorption and passage of all four EDCs increase with hydrophobicity (expressed as K_{ow}) instead of molecular weight, confirming the presence of hydrophobic interactions that has potentially jeopardized the rejection of hydrophobic OMPs. Nevertheless, the electrostatic repulsion effects might counteract such unfavorable influence when the solute is charged and the membrane pore size is sufficiently small compared to the solute. For instance, as shown in **Fig. 5b**, the rejection of negatively charged PFASs by TFNi membrane was slightly higher than the SE curve including the relatively hydrophobic PFOA and PFOS (see K_{ow} in **Table 1**). Since the surface charge of TFNi membrane is also negative, the electrostatic repulsion takes place to diminish the approach of PFASs to the membrane surface, thus reducing the adsorption onto, and subsequent partitioning into membrane, giving rise to higher rejection of PFASs than those uncharged molecular probes (Steinle-Darling and Reinhard, 2008; Verliefde et al., 2008). For the TFC membrane with negative surface charge similar to TFNi membrane (**Fig.S4b**), the electrostatic interactions also play a role in making the rejection of several PFASs higher than neutral molecules (**Fig. 5a**). However, the rejection of PFOA and PFOS fell below the SE curve, indicating the electrostatic repulsion was weaker than hydrophobic interactions. This is likely attributed to the large pore size of TFC membrane that might reduce electrostatic repulsion (Wang and Lin, 2021) and meanwhile increase the internal pore sorption of hydrophobic OMPs (Semião and Schäfer, 2013) (see the higher sorption of PFOA and PFOS by TFC membrane compared to TFNi membrane in **Fig. S9**). To better understand the combined effects of size exclusion and charge interaction, Yang et al. (Yang et al., 2017) introduced an effective molecular size (r_{eff}): $r_{eff} = r_s + k \cdot \Lambda_d$, where r_s is the Stokes radius accounting for size exclusion effect and k is a proportionality constant accounting for electrostatic

interaction through the Debye length λ_d. According to these authors, the overall rejection is governed by the ratio of the effective molecular size over the membrane pore size.

In addition to the size exclusion effects, hydrophobic interactions, and electrostatic interactions, the rejection of OMPs by TFC and TFNi membranes could also be influenced by structural effects. For example, the rejection of two PhACs (i.e., SMX and SDZ) was apparently lower than the surrogates with similar properties of size, charge, and hydrophilicity. This might be ascribed to the structural difference as displayed in **Fig. 5c** that PhACs have cylindrical/linear structure whereas the surrogates possess near-spherical shape. Since the Stokes radius is calculated assuming sphere solutes (Deen, 1987), the actual size of PhACs would differ from neutral molecule probes even of the same Stokes radius. Moreover, the SMX and SDZ are relatively polar (Nghiem et al., 2005). It is therefore easier for these two linear PhACs to usher through the membrane pores with polar interactions, resulting in lower rejection. In contrast to the linear flexible molecules SMX and SDZ, PFASs such as PFOS and PFOA have a rigid backbone despite their linear structure, which might explain their better rejections compared to SMX and SDZ. In addition, the negatively charged PFASs also benefit from the electrostatic repulsion by the negatively charged membrane surface as discussed earlier.

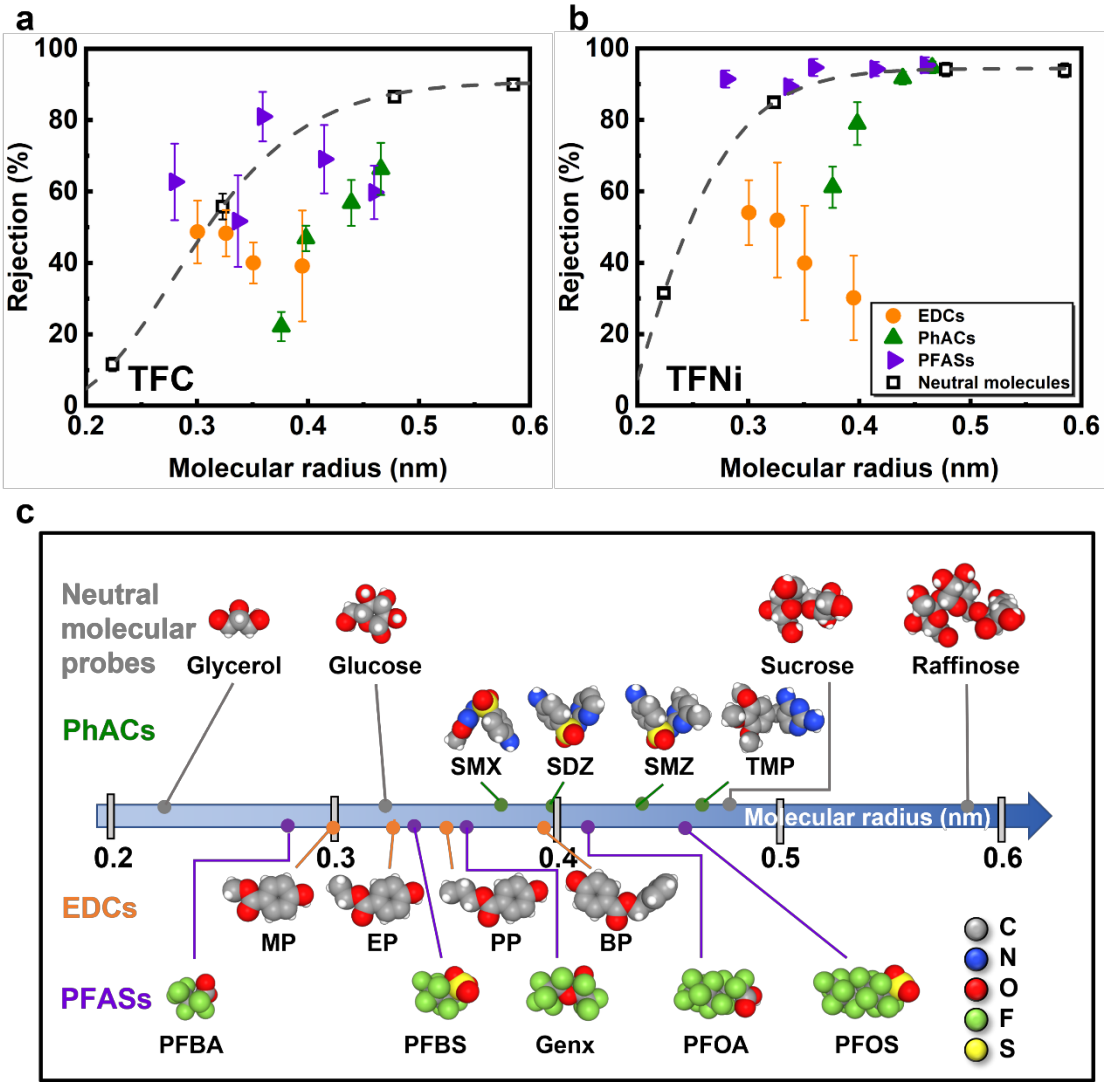

Fig. 5. Rejection of EDCs, PhACs, PFASs, and neutral molecules by (a) TFC membrane and (b) TFNi membrane correlated with solute molecular radius. Dash lines represent the rejection trend of neutral molecules fitted by using log-normal cumulative density function. (c) Solute properties including structural and size information. The 3D structures were obtained from U.S. National Library of Medicine (https://pubchem.ncbi.nlm.nih.gov/). For OMPs rejection experiments, a cocktail of three types of OMPs were added (200 μg/L, pH 7 ± 0.5, 25 °C) with 600 mg/L NaCl as background. For neutral molecules filtration experiment, feed solution contained single solute (200 mg/L, pH 7 ± 0.5, 25 °C). All the measurements were triplicated under the applied pressure of 5 bar at crossflow velocity of 16.7 cm/s.

Besides the interactions between OMPs and membranes as discussed before, to investigate whether TFNi membrane has enhanced the OMPs selectivity and how it works, we further compared the water-solute selectivity (*A*/*B*) of TFC and TFNi membranes (**Fig. 6**). We found the selectivity of EDCs (**Fig. 6a**) remained almost unchanged whereas that of PhACs (**Fig. 6b**), PFASs (**Fig. 6c**), and neutral molecular probes (**Fig. 6d**) was significantly improved after incorporating interlayer. To understand whether the selectivity of the interlayer itself plays an important role in the rejection behavior of the TFNi membrane, we also compared the selectivity of TFC and TFNi membranes to that of an Fe/TA layer (**Supplementary materials S10**). Despite a previous work (Guo et al., 2019) showing that the hydrophilic Fe/TA layer has relatively high selectivity against hydrophobic EDCs such as MP, EP, PP, and BP, the TFNi membrane in the current study did not show systematically enhanced rejection of EDCs. This result seems to suggest that the polyamide rejection layer plays a more important role than the Fe/TA interlayer with respect to the rejection of EDCs, although the effectiveness of including a highly selective interlayer deserves further investigation in future studies.

Accordingly, in terms of the underlying mechanism, the result presented in **Fig. 6** can be interpreted from two major aspects (see schematic illustration in **Table 3**). For one thing, the water permeance (*A*) of TFNi membrane has increased due to (1) gutter effect of interlayer, (2) less structural deformation of substrate during heat treatment as demonstrated in **Section 3.2**, and (3) less resistance from the thinner and crumpled polyamide layer containing nanovoids. For another, the solute permeance (*B*) is greatly affected by the better formed polyamide layer. Specifically, the polyamide layer of TFNi membrane in this study was denser, better cross-linked and possessed smaller average pore size with narrower distribution, which is beneficial to enhance size

exclusion effects thus reducing *B* value. Moreover, as stated previously, the electrostatic repulsion might be enhanced as the membrane pore size becomes smaller, in which case there would be synergic effects on reducing OMPs permeance. This may explain why the selectivity improvement of charged PFASs by TFNi membrane was even higher than that of neutral molecular probes of similar size. However, for those small and hydrophobic EDCs, the selectivity enhancement was not obvious, which indicates the unfavorable hydrophobic interactions were predominant in both TFC and TFNi membranes. According to literature (Guo et al., 2019), the selectivity of these four EDCs by the tight XLE membrane or non-polyamide based nanofiltration membrane was relatively high. In view of this, to further improve the selectivity towards EDCs, optimization of the formula of interlayer might be required to endow the membrane with sufficiently small pore size, or the polyamide chemistry could be substituted with novel materials to suppress hydrophobic interactions with EDCs.

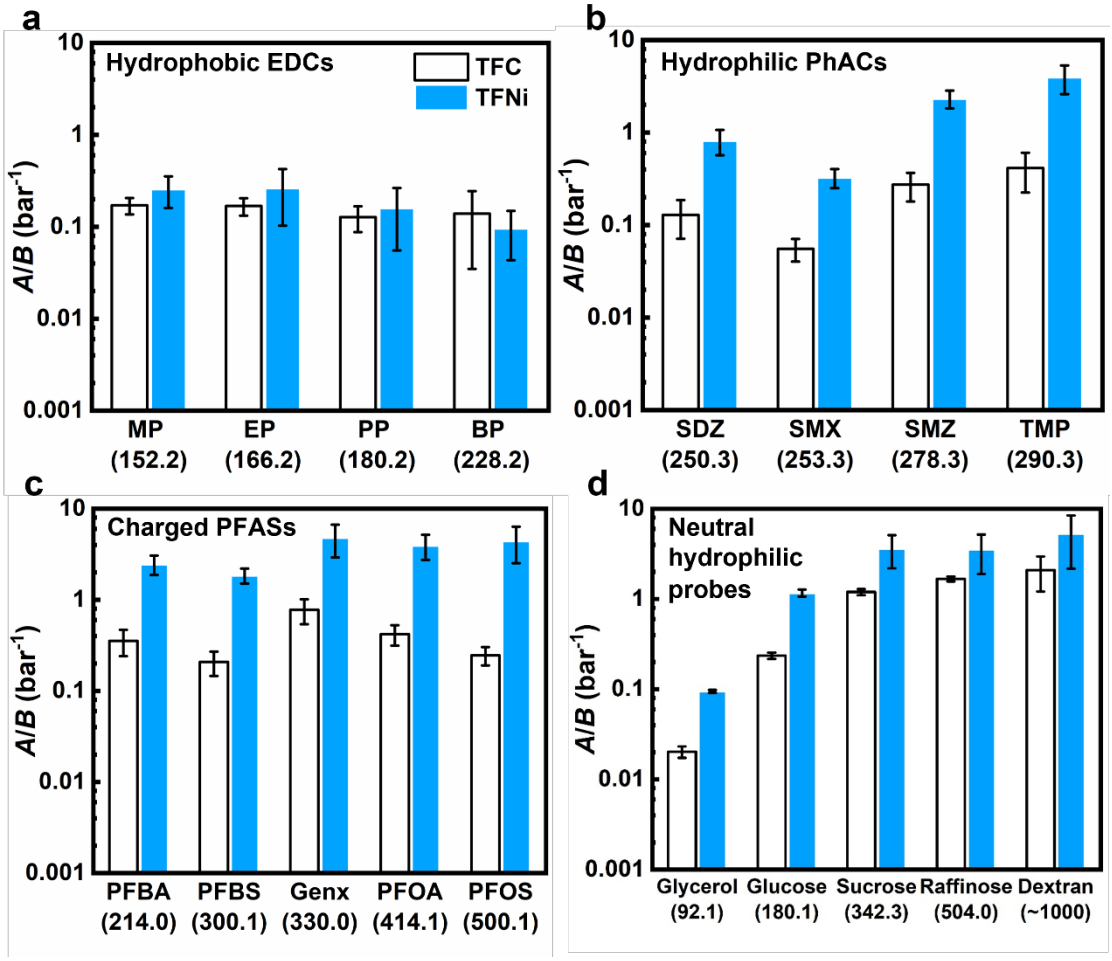

Fig. 6. Water-solute selectivity (*A*/*B*) of (a) hydrophobic EDCs, (b) hydrophilic PhACs, (c) negatively charged PFASs, and (d) neutral hydrophilic molecular probes by TFC and TFNi membranes. In each graph, solutes are listed following the order of molecular weight as annotated in bracket. Error bars were obtained from at least three filtration experiments.

473 **Table 3**

474 Mechanism of enhanced membrane selectivity.

Effects of interlayer on membrane structure/property/performance	**Schematic illustration**	**Influence on membrane selectivity**	**References**
<u>Gutter effect</u> • Permeable gutter layer serving as the receiving end of water from polyamide layer. • Shortened lateral water transport distance in the less permeable polyamide layer. • Enhanced water permeance due to reduced overall water resistance.	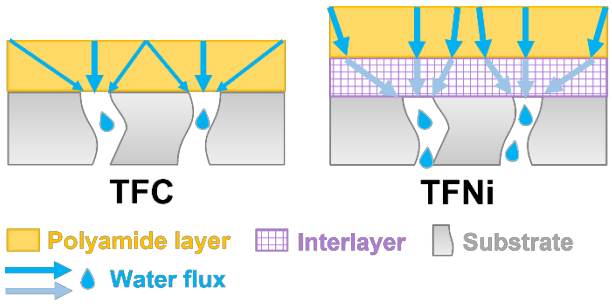	Increased water permeance.	(Long et al., 2022; Wang et al., 2022; Yang et al., 2020b)
<u>Resisting potential structural deformation of substrate</u> • Less pore shrinkage of substrate. • Minimized funnel effect where water has to transport longer distance to reach the permeable pores of substrate. • Enhanced water permeance due to lower resistance.	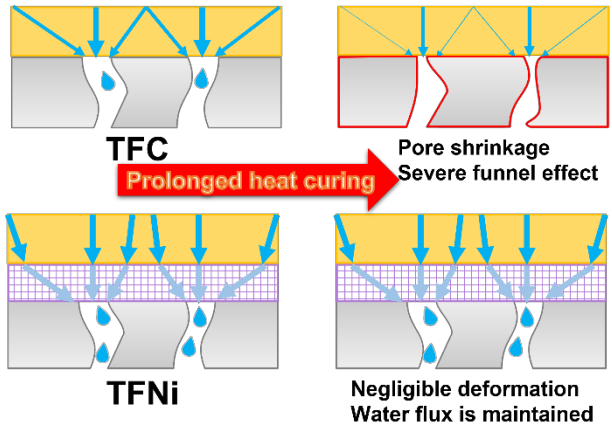	Increased water permeance.	(Wang et al., 2022; Zhan et al., 2020b)
<u>Thinner and crumpled polyamide layer containing nanovoids</u> • More effective filtration area with less resistance. • Self-guttering effect optimizing water transport pathways. • Enhanced water permeance.	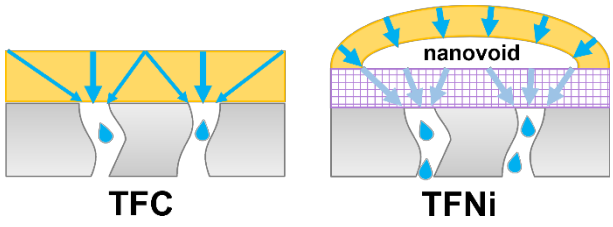	Increased water permeance.	(Hu et al., 2023; Shao et al., 2022; Tan et al., 2018)
<u>Facilitating better formation of polyamide layer</u> • Higher cross-linking degree and denser polyamide layer, smaller average pore size with narrower distribution. • Enhanced size exclusion effect and electrostatic interaction due to smaller pore size. • Reduced solute permeance.	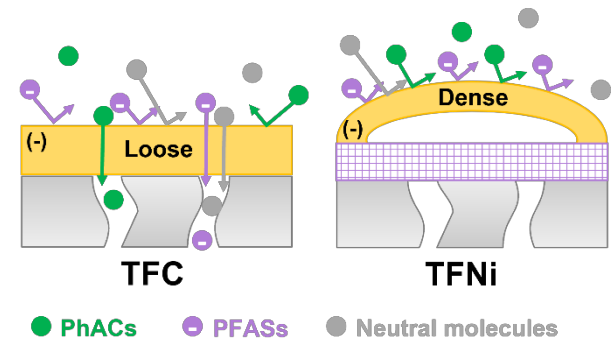	Reduced permeance to PhACs, PFASs, and neutral molecular probes.	(Yang et al., 2020b; Yang et al., 2018; Zhang et al., 2020)

4. Conclusions

In this work, we performed IP reaction with 0.2 wt% PIP and 0.1 wt% TMC onto PSf substrate to fabricate TFC membrane and chose Fe (III)–tannic acid as an interlayer to prepare TFNi membrane. Different from the pristine TFC membrane, the TFNi membrane presented crumpled morphology and its rejection layer was denser, better cross-linked and possessed smaller average pore size with narrower distribution. After introducing interlayer, the water permeance was doubled probably due to gutter effect, smaller water resistance from the thinner and crumpled polyamide layer, and less pore shrinkage of substrate during heat-curing process. We found there were several mechanisms affecting the rejection of OMPs by TFC and TFNi membranes apart from the dominant size exclusion effects. The significant enhancement in water-OMPs selectivity (A/B) of PhACs and PFASs was attributed to the effects of interlayer in increasing membrane permeance to water (A value) and meanwhile decreasing permeance to OMPs (B value) by enhancing size exclusion effects. To further improve the selectivity of water/EDCs, membrane structure and chemistry should be tuned to enhance size exclusion and suppress hydrophobic interactions at the same time.

Acknowledgements

This work was supported by Guangdong-Hong Kong Technology Cooperation Funding Scheme under the Innovation and Technology Fund of Hong Kong (GHP/181/20GD) and Science and Technology Planning Project of Guangdong Province (2021A0505110013). The work was also partially supported by the grant from the Research Grants Council of the Hong Kong Special Administration Region, China (GRF 17201921). We want to extend great gratitude to Dr. Chan Y. F. and Dr. Wong H. M. of the Electron Microscope Unit of the University of Hong Kong (HKU) for the STEM test. We appreciate the training of using LC-MS/MS from Ms. Chu H. of the School of Biological Sciences, HKU. We also thank Mr. Chan T. O. of the Department of Civil Engineering, HKU for making the cross-flow nanofiltration setup.

References

Barbosa, M.O., Moreira, N.F., Ribeiro, A.R., Pereira, M.F., Silva, A.M., 2016. Occurrence and removal of organic micropollutants: An overview of the watch list of EU Decision 2015/495. Water Res. 94, 257-279.

Bellona, C., Drewes, J.E., Xu, P., Amy, G., 2004. Factors affecting the rejection of organic solutes during NF/RO treatment—a literature review. Water Res. 38 (12), 2795-2809.

Ben-David, A., Bernstein, R., Oren, Y., Belfer, S., Dosoretz, C., Freger, V., 2010. Facile surface modification of nanofiltration membranes to target the removal of endocrine-disrupting compounds. J. Membr. Sci. 357 (1-2), 152-159.

Ben, W., Zhu, B., Yuan, X., Zhang, Y., Yang, M., Qiang, Z., 2018. Occurrence, removal and risk of organic micropollutants in wastewater treatment plants across China: Comparison of wastewater treatment processes. Water Res. 130, 38-46.

Dai, R., Guo, H., Tang, C.Y., Chen, M., Li, J., Wang, Z., 2019. Hydrophilic selective nanochannels created by metal organic frameworks in nanofiltration membranes enhance rejection of hydrophobic endocrine-disrupting compounds. Environ. Sci. Technol. 53 (23), 13776-13783.

Dai, R., Li, J., Wang, Z., 2020. Constructing interlayer to tailor structure and performance of thin-film composite polyamide membranes: A review. Adv. Colloid Interface Sci. 282, 102204.

Deen, W., 1987. Hindered transport of large molecules in liquid-filled pores. AlChE J. 33 (9), 1409-1425.

Do, V.T., Tang, C.Y., Reinhard, M., Leckie, J.O., 2012. Degradation of polyamide nanofiltration and reverse osmosis membranes by hypochlorite. Environ. Sci. Technol. 46 (2), 852-859.

Fane, A., Tang, C., Wang, R., 2011. Treatise on water science. Elsevier, Oxford, pp. 301-335.

Fent, K., Weston, A.A., Caminada, D., 2006. Ecotoxicology of human pharmaceuticals. Aquat. Toxicol. 76 (2), 122-159.

Gao, S., Zhu, Y., Gong, Y., Wang, Z., Fang, W., Jin, J., 2019. Ultrathin polyamide nanofiltration membrane fabricated on brush-painted single-walled carbon nanotube network support for ion sieving. ACS nano 13 (5), 5278-5290.

Guo, H., Dai, R., Xie, M., Peng, L.E., Yao, Z., Yang, Z., Nghiem, L.D., Snyder, S.A., Wang, Z., Tang, C.Y., 2022. Tweak in Puzzle: Tailoring Membrane Chemistry and Structure toward Targeted Removal of Organic Micropollutants for Water Reuse. Environ. Sci. Technol. Lett. 9 (4), 247-257.

Guo, H., Deng, Y., Tao, Z., Yao, Z., Wang, J., Lin, C., Zhang, T., Zhu, B., Tang, C.Y., 2016. Does hydrophilic polydopamine coating enhance membrane rejection of hydrophobic endocrine-disrupting compounds? Environ. Sci. Technol. Lett. 3 (9), 332-338.

Guo, H., Deng, Y., Yao, Z., Yang, Z., Wang, J., Lin, C., Zhang, T., Zhu, B., Tang, C.Y., 2017a. A highly selective surface coating for enhanced membrane rejection of endocrine disrupting compounds: Mechanistic insights and implications. Water Res. 121, 197-203.

Guo, H., Li, X., Yang, W., Yao, Z., Mei, Y., Peng, L.E., Yang, Z., Shao, S., Tang, C.Y., 2021a. Nanofiltration for drinking water treatment: a review. Front. Chem. Sci. Eng., 1-18.

Guo, H., Peng, L.E., Yao, Z., Yang, Z., Ma, X., Tang, C.Y., 2019. Non-polyamide based nanofiltration membranes using green metal–organic coordination complexes: implications for the removal of trace organic contaminants. Environ. Sci. Technol. 53 (5), 2688-2694.

Guo, H., Yao, Z., Yang, Z., Ma, X., Wang, J., Tang, C.Y., 2017b. A one-step rapid assembly of thin film coating using green coordination complexes for enhanced removal of trace organic contaminants by membranes. Environ. Sci. Technol. 51 (21), 12638-12643.

Guo, H., Zhang, J., Peng, L.E., Li, X., Chen, Y., Yao, Z., Fan, Y., Shih, K., Tang, C.Y., 2021b. High-

efficiency capture and recovery of anionic perfluoroalkyl substances from water using PVA/PDDA nanofibrous membranes with near-zero energy consumption. Environ. Sci. Technol. Lett. 8 (4), 350-355.

Heredia-Guerrero, J.A., Benítez, J.J., Domínguez, E., Bayer, I.S., Cingolani, R., Athanassiou, A., Heredia, A., 2014. Infrared and Raman spectroscopic features of plant cuticles: a review. Front. Plant Sci. 5, 305.

Houtz, E.F., Higgins, C.P., Field, J.A., Sedlak, D.L., 2013. Persistence of perfluoroalkyl acid precursors in AFFF-impacted groundwater and soil. Environ. Sci. Technol. 47 (15), 8187-8195.

Hu, Y., Wang, F., Yang, Z., Tang, C.Y., 2023. Modeling nanovoid-enhanced water permeance of thin film composite membranes. J. Membr. Sci., 121555.

Huang, S., McDonald, J.A., Kuchel, R.P., Khan, S.J., Leslie, G., Tang, C.Y., Mansouri, J., Fane, A.G., 2021. Surface modification of nanofiltration membranes to improve the removal of organic micropollutants: Linking membrane characteristics to solute transmission. Water Res. 203, 117520.

Jin, X., Hu, J., Ong, S.L., 2010. Removal of natural hormone estrone from secondary effluents using nanofiltration and reverse osmosis. Water Res. 44 (2), 638-648.

Karan, S., Jiang, Z., Livingston, A.G., 2015. Sub–10 nm polyamide nanofilms with ultrafast solvent transport for molecular separation. Science 348 (6241), 1347-1351.

Kim, J.-H., Park, P.-K., Lee, C.-H., Kwon, H.-H., 2008. Surface modification of nanofiltration membranes to improve the removal of organic micro-pollutants (EDCs and PhACs) in drinking water treatment: Graft polymerization and cross-linking followed by functional group substitution. J. Membr. Sci. 321 (2), 190-198.

Krafft, M.P., Riess, J.G., 2015. Per-and polyfluorinated substances (PFASs): Environmental challenges. Curr. Opin. Colloid Interface Sci. 20 (3), 192-212.

Lapworth, D., Baran, N., Stuart, M., Ward, R., 2012. Emerging organic contaminants in groundwater: a review of sources, fate and occurrence. Environ. Pollut. 163, 287-303.

Lau, W., Gray, S., Matsuura, T., Emadzadeh, D., Chen, J.P., Ismail, A., 2015. A review on polyamide thin film nanocomposite (TFN) membranes: History, applications, challenges and approaches. Water Res. 80, 306-324.

Lau, W., Ismail, A., Misdan, N., Kassim, M., 2012. A recent progress in thin film composite membrane: A review. Desalination 287, 190-199.

Li, Y., Su, Y., Li, J., Zhao, X., Zhang, R., Fan, X., Zhu, J., Ma, Y., Liu, Y., Jiang, Z., 2015. Preparation of thin film composite nanofiltration membrane with improved structural stability through the mediation of polydopamine. J. Membr. Sci. 476, 10-19.

Long, L., Wu, C., Yang, Z., Tang, C.Y., 2022. Carbon Nanotube Interlayer Enhances Water Permeance and Antifouling Performance of Nanofiltration Membranes: Mechanisms and Experimental Evidence. Environ. Sci. Technol. 56 (4), 2656-2664.

Luo, Y., Guo, W., Ngo, H.H., Nghiem, L.D., Hai, F.I., Zhang, J., Liang, S., Wang, X.C., 2014. A review on the occurrence of micropollutants in the aquatic environment and their fate and removal during wastewater treatment. Sci. Total Environ. 473, 619-641.

Ma, X.-H., Yang, Z., Yao, Z.-K., Xu, Z.-L., Tang, C.Y., 2017. A facile preparation of novel positively charged MOF/chitosan nanofiltration membranes. J. Membr. Sci. 525, 269-276.

Miyashita, Y., Park, S.-H., Hyung, H., Huang, C.-H., Kim, J.-H., 2009. Removal of N-nitrosamines and their precursors by nanofiltration and reverse osmosis membranes. J. Environ. Eng. 135 (9), 788-795.

Nghiem, L.D., Schäfer, A.I., 2002. Adsorption and transport of trace contaminant estrone in NF/RO

membranes. Environ. Eng. Sci. 19 (6), 441-451.
Nghiem, L.D., Schäfer, A.I., Elimelech, M., 2004. Removal of natural hormones by nanofiltration membranes: measurement, modeling, and mechanisms. Environ. Sci. Technol. 38 (6), 1888-1896.
Nghiem, L.D., Schäfer, A.I., Elimelech, M., 2005. Pharmaceutical retention mechanisms by nanofiltration membranes. Environ. Sci. Technol. 39 (19), 7698-7705.
Petrie, B., Barden, R., Kasprzyk-Hordern, B., 2015. A review on emerging contaminants in wastewaters and the environment: current knowledge, understudied areas and recommendations for future monitoring. Water Res. 72, 3-27.
Sarango, L., Paseta, L., Navarro, M., Zornoza, B., Coronas, J., 2018. Controlled deposition of MOFs by dip-coating in thin film nanocomposite membranes for organic solvent nanofiltration. J. Ind. Eng. Chem. 59, 8-16.
Schäfer, A.I., Akanyeti, I., Semião, A.J., 2011. Micropollutant sorption to membrane polymers: a review of mechanisms for estrogens. Adv. Colloid Interface Sci. 164 (1-2), 100-117.
Schmidt, W., O'Rourke, K., Hernan, R., Quinn, B., 2011. Effects of the pharmaceuticals gemfibrozil and diclofenac on the marine mussel (Mytilus spp.) and their comparison with standardized toxicity tests. Mar. Pollut. Bull. 62 (7), 1389-1395.
Schwarzenbach, R.P., Escher, B.I., Fenner, K., Hofstetter, T.B., Johnson, C.A., Von Gunten, U., Wehrli, B., 2006. The challenge of micropollutants in aquatic systems. Science 313 (5790), 1072-1077.
Semião, A.J., Schäfer, A.I., 2013. Removal of adsorbing estrogenic micropollutants by nanofiltration membranes. Part A—Experimental evidence. J. Membr. Sci. 431, 244-256.
Shannon, M.A., Bohn, P.W., Elimelech, M., Georgiadis, J.G., Marinas, B.J., Mayes, A.M., 2008. Science and technology for water purification in the coming decades. Nature 452 (7185), 301-310.
Shao, S., Zeng, F., Long, L., Zhu, X., Peng, L.E., Wang, F., Yang, Z., Tang, C.Y., 2022. Nanofiltration membranes with crumpled polyamide films: a critical review on mechanisms, performances, and environmental applications. Environ. Sci. Technol. 56 (18), 12811-12827.
Souza, M.S., Hallgren, P., Balseiro, E., Hansson, L.-A., 2013. Low concentrations, potential ecological consequences: synthetic estrogens alter life-history and demographic structures of aquatic invertebrates. Environ. Pollut. 178, 237-243.
Steinle-Darling, E., Reinhard, M., 2008. Nanofiltration for trace organic contaminant removal: structure, solution, and membrane fouling effects on the rejection of perfluorochemicals. Environ. Sci. Technol. 42 (14), 5292-5297.
Steinle-Darling, E., Zedda, M., Plumlee, M.H., Ridgway, H.F., Reinhard, M., 2007. Evaluating the impacts of membrane type, coating, fouling, chemical properties and water chemistry on reverse osmosis rejection of seven nitrosoalklyamines, including NDMA. Water Res. 41 (17), 3959-3967.
Tan, Z., Chen, S., Peng, X., Zhang, L., Gao, C., 2018. Polyamide membranes with nanoscale Turing structures for water purification. Science 360 (6388), 518-521.
Tang, C.Y., Fu, Q.S., Robertson, A., Criddle, C.S., Leckie, J.O., 2006. Use of reverse osmosis membranes to remove perfluorooctane sulfonate (PFOS) from semiconductor wastewater. Environ. Sci. Technol. 40 (23), 7343-7349.
Tang, C.Y., Kwon, Y.-N., Leckie, J.O., 2007a. Characterization of humic acid fouled reverse osmosis and nanofiltration membranes by transmission electron microscopy and streaming potential measurements. Environ. Sci. Technol. 41 (3), 942-949.
Tang, C.Y., Kwon, Y.-N., Leckie, J.O., 2007b. Probing the nano-and micro-scales of reverse osmosis membranes—A comprehensive characterization of physiochemical properties of uncoated and coated

membranes by XPS, TEM, ATR-FTIR, and streaming potential measurements. J. Membr. Sci. 287 (1), 146-156.
Tang, C.Y., Kwon, Y.-N., Leckie, J.O., 2009. Effect of membrane chemistry and coating layer on physiochemical properties of thin film composite polyamide RO and NF membranes: I. FTIR and XPS characterization of polyamide and coating layer chemistry. Desalination 242 (1-3), 149-167.
Tang, C.Y., Yang, Z., Guo, H., Wen, J.J., Nghiem, L.D., Cornelissen, E., 2018. Potable water reuse through advanced membrane technology. Environ. Sci. Technol. 52 (18), 10215-10223.
Tran, N.H., Reinhard, M., Gin, K.Y.-H., 2018. Occurrence and fate of emerging contaminants in municipal wastewater treatment plants from different geographical regions-a review. Water Res. 133, 182-207.
Van der Bruggen, B., Vandecasteele, C., 2002. Modelling of the retention of uncharged molecules with nanofiltration. Water Res. 36 (5), 1360-1368.
Verliefde, A.R., Cornelissen, E., Heijman, S., Verberk, J., Amy, G., Van der Bruggen, B., Van Dijk, J., 2008. The role of electrostatic interactions on the rejection of organic solutes in aqueous solutions with nanofiltration. J. Membr. Sci. 322 (1), 52-66.
Verliefde, A.R.D., Cornelissen, E.R., Heijman, S.G.J., Hoek, E.M.V., Amy, G.L., Bruggen, B.V.d., van Dijk, J.C., 2009. Influence of Solute−Membrane Affinity on Rejection of Uncharged Organic Solutes by Nanofiltration Membranes. Environ. Sci. Technol. 43 (7), 2400-2406.
Wang, F., Yang, Z., Tang, C.Y., 2022. Modeling Water Transport in Interlayered Thin-Film Nanocomposite Membranes: Gutter Effect vs Funnel Effect. ACS ES&T Eng. 2 (11), 2023-2033.
Wang, R., Lin, S., 2021. Pore model for nanofiltration: History, theoretical framework, key predictions, limitations, and prospects. J. Membr. Sci. 620, 118809.
Wang, S., Li, L., Yu, S., Dong, B., Gao, N., Wang, X., 2021. A review of advances in EDCs and PhACs removal by nanofiltration: Mechanisms, impact factors and the influence of organic matter. Chem. Eng. J. 406, 126722.
Wang, X.-m., Li, B., Zhang, T., Li, X.-y., 2015. Performance of nanofiltration membrane in rejecting trace organic compounds: Experiment and model prediction. Desalination 370, 7-16.
Warsinger, D.M., Chakraborty, S., Tow, E.W., Plumlee, M.H., Bellona, C., Loutatidou, S., Karimi, L., Mikelonis, A.M., Achilli, A., Ghassemi, A., 2018. A review of polymeric membranes and processes for potable water reuse. Prog. Polym. Sci. 81, 209-237.
Williams, R.J., Johnson, A.C., Smith, J.J., Kanda, R., 2003. Steroid estrogens profiles along river stretches arising from sewage treatment works discharges. Environ. Sci. Technol. 37 (9), 1744-1750.
Wilson, D., Langell, M., 2014. XPS analysis of oleylamine/oleic acid capped Fe3O4 nanoparticles as a function of temperature. Appl. Surf. Sci. 303, 6-13.
Yang, L., She, Q., Wan, M.P., Wang, R., Chang, V.W.-C., Tang, C.Y., 2017. Removal of haloacetic acids from swimming pool water by reverse osmosis and nanofiltration. Water Res. 116, 116-125.
Yang, W., Long, L., Guo, H., Wu, C., Zhou, S., Mei, Y., Peng, L.E., Liu, W., Yang, Z., Li, W., 2022. Facile synthesis of nanofiltration membrane with asymmetric selectivity towards enhanced water recovery for groundwater remediation. J. Membr. Sci., 121038.
Yang, Z., Guo, H., Tang, C.Y., 2019a. The upper bound of thin-film composite (TFC) polyamide membranes for desalination. J. Membr. Sci. 590, 117297.
Yang, Z., Guo, H., Yao, Z.-k., Mei, Y., Tang, C.Y., 2019b. Hydrophilic silver nanoparticles induce selective nanochannels in thin film nanocomposite polyamide membranes. Environ. Sci. Technol. 53 (9), 5301-5308.

Yang, Z., Sun, P.-F., Li, X., Gan, B., Wang, L., Song, X., Park, H.-D., Tang, C.Y., 2020a. A critical review on thin-film nanocomposite membranes with interlayered structure: mechanisms, recent developments, and environmental applications. Environ. Sci. Technol. 54 (24), 15563-15583.

Yang, Z., Wang, F., Guo, H., Peng, L.E., Ma, X.-h., Song, X.-x., Wang, Z., Tang, C.Y., 2020b. Mechanistic insights into the role of polydopamine interlayer toward improved separation performance of polyamide nanofiltration membranes. Environ. Sci. Technol. 54 (18), 11611-11621.

Yang, Z., Zhou, Z.-w., Guo, H., Yao, Z., Ma, X.-h., Song, X., Feng, S.-P., Tang, C.Y., 2018. Tannic acid/Fe3+ nanoscaffold for interfacial polymerization: toward enhanced nanofiltration performance. Environ. Sci. Technol. 52 (16), 9341-9349.

Yuan, B., Zhao, S., Hu, P., Cui, J., Niu, Q.J., 2020. Asymmetric polyamide nanofilms with highly ordered nanovoids for water purification. Nat. Commun. 11 (1), 6102.

Yuan, J., Wu, M., Wu, H., Liu, Y., You, X., Zhang, R., Su, Y., Yang, H., Shen, J., Jiang, Z., 2019. Covalent organic framework-modulated interfacial polymerization for ultrathin desalination membranes. J. Mater. Chem. A 7 (44), 25641-25649.

Zhai, Z., Jiang, C., Zhao, N., Dong, W., Lan, H., Wang, M., Niu, Q.J., 2018. Fabrication of advanced nanofiltration membranes with nanostrand hybrid morphology mediated by ultrafast Noria–polyethyleneimine codeposition. J. Mater. Chem. A 6 (42), 21207-21215.

Zhan, Z.-M., Xu, Z.-L., Zhu, K.-K., Tang, Y.-J., 2020a. How to understand the effects of heat curing conditions on the morphology and performance of polypiperazine-amide NF membrane. J. Membr. Sci. 597, 117640.

Zhan, Z.-M., Xu, Z.-L., Zhu, K.-K., Xue, S.-M., Ji, C.-H., Huang, B.-Q., Tang, C.Y., Tang, Y.-J., 2020b. Superior nanofiltration membranes with gradient cross-linked selective layer fabricated via controlled hydrolysis. J. Membr. Sci. 604, 118067.

Zhang, M., Jin, W., Yang, F., Duke, M., Dong, Y., Tang, C.Y., 2020. Engineering a nanocomposite interlayer for a novel ceramic-based forward osmosis membrane with enhanced performance. Environ. Sci. Technol. 54 (12), 7715-7724.

Zhang, X., Lv, Y., Yang, H.-C., Du, Y., Xu, Z.-K., 2016. Polyphenol coating as an interlayer for thin-film composite membranes with enhanced nanofiltration performance. ACS Appl. Mater. Interfaces 8 (47), 32512-32519.

Zhao, Y.-y., Liu, Y.-l., Wang, X.-m., Huang, X., Xie, Y.F., 2019. Impacts of metal–organic frameworks on structure and performance of polyamide thin-film nanocomposite membranes. ACS Appl. Mater. Interfaces 11 (14), 13724-13734.

Zhao, Y., Tong, X., Chen, Y., 2021. Fit-for-purpose design of nanofiltration membranes for simultaneous nutrient recovery and micropollutant removal. Environ. Sci. Technol. 55 (5), 3352-3361.

Zhou, S., Long, L., Yang, Z., So, S.L., Gan, B., Guo, H., Feng, S.-P., Tang, C.Y., 2022. Unveiling the Growth of Polyamide Nanofilms at Water/Organic Free Interfaces: Toward Enhanced Water/Salt Selectivity. Environ. Sci. Technol. 56 (14), 10279-10288.

Supplementary materials

Enhancing the removal of organic micropollutants by nanofiltration membrane with Fe (III)–tannic acid interlayer: Mechanisms and environmental implications

Wenyu Liu [a], Li Long [a], Zhe Yang [a], Li Wang [a], Qimao Gan [a], Shenghua Zhou [a], Pulak Sarkar [a], Hao Guo [b,*], Chuyang Y. Tang [a,*]

[a] Department of Civil Engineering, The University of Hong Kong, Pokfulam, Hong Kong SAR, China

[b] Institute of Environment and Ecology, Tsinghua Shenzhen International Graduate School, Tsinghua University, Shenzhen 518055, China

* Corresponding authors

Hao Guo (ORCID: 0000-0002-0688-5431)

Tel: +86 15889350923

E-mail: guohao@sz.tsinghua.edu.cn

Chuyang Y. Tang (ORCID: 0000-0002-7932-6462)

Tel: +852 2859 1976

E-mail: tangc@hku.hk

Number of pages (including the cover page): 16

Number of figures: 11

Number of tables: 2

Page 3 S1. Cross-flow nanofiltration setup

Page 4 S2. Comparison of OMPs rejection at different equilibrium time

Page 5 S3. Membrane characterization results

Page 8 S4. Estimation of enhancement of water permeance

Page 10 S5. Membrane separation performance

Page 11 S6. Estimation of membrane pore size

Page 12 S7. OMPs rejection by membranes with different heat treatment duration

Page 13 S8. Sorption of OMPs onto NF membranes

Page 14 S9. Passage and sorption of EDCs by TFC and TFNi membranes

Page 15 S10. OMPs selectivity of an Fe/TA layer

S1. Cross-flow nanofiltration setup

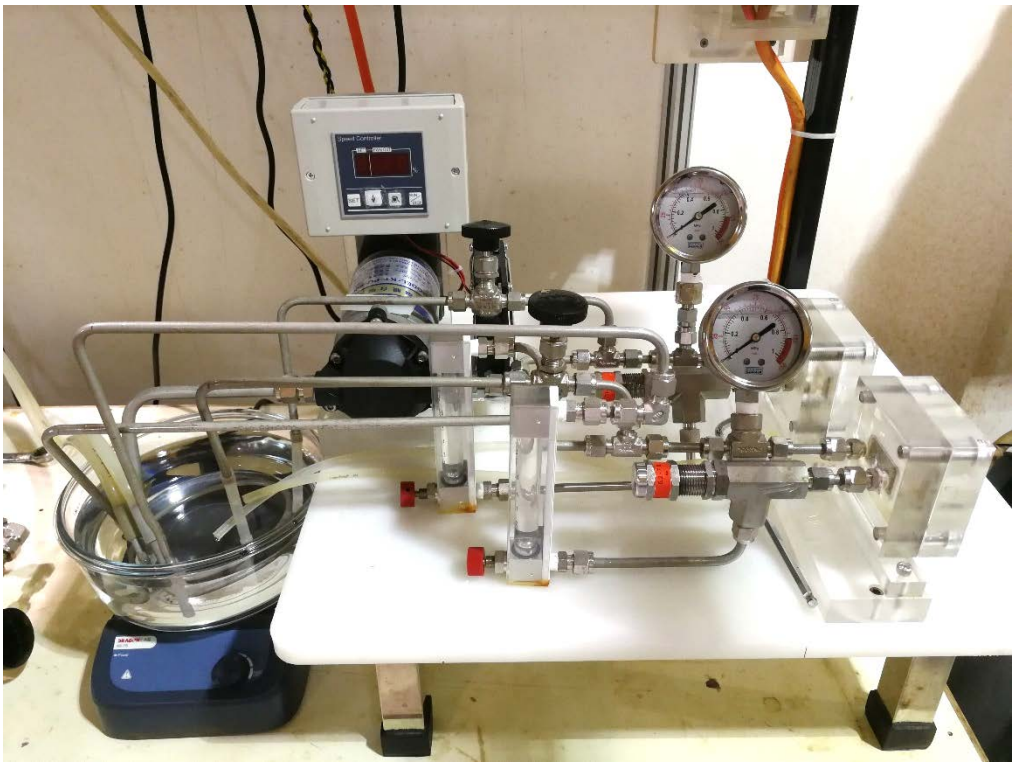

Fig. S1. Photo of cross-flow nanofiltration setup. During the filtration experiment, feed solution was drawn by a diaphragm self-priming pump (KT-PU-400G, Kerter, China) to two paralleled membrane cells made of polymethyl methacrylate (PMMA), each with an effective filtration area of 8 cm^2 and a slit depth of 2.5 mm. Spacers were imbedded inside the slit to generate cross flow. Retentate was circulated back into feed through stainless steel pipes. Testing temperature was maintained at 25 ℃ by a cooling system (ALGY-II, AOLINGHENGYE, China).

S2. Comparison of OMPs rejection at different equilibrium time

We performed some preliminary tests to compare the rejection of OMPs at different equilibrium time (6 h vs. 18 h). No major difference was observed for rejection measured at the two different durations, suggesting that the 6 h exposure to OMPs is reasonable to achieve a stable rejection performance.

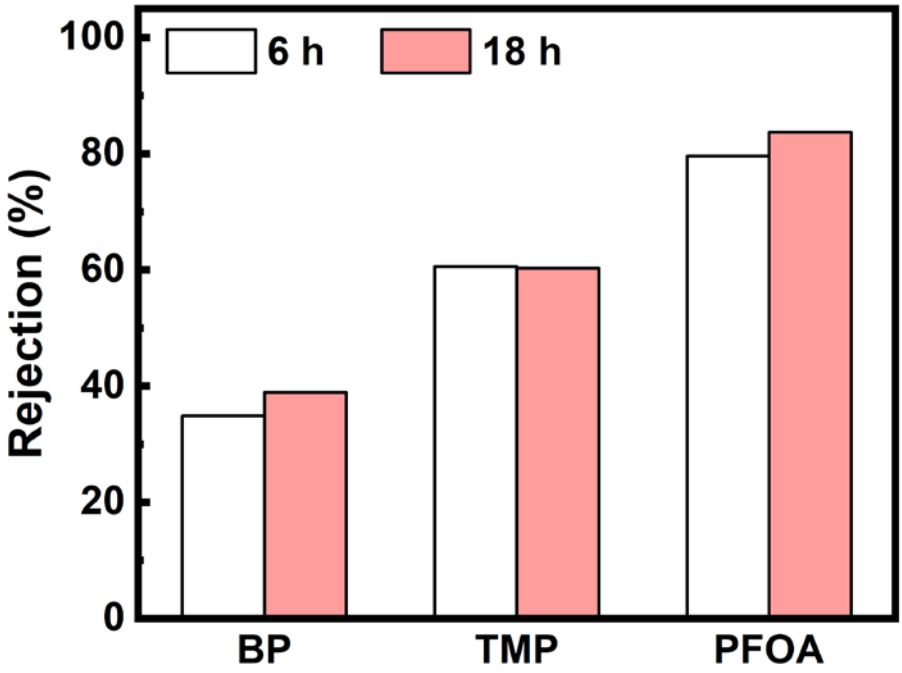

Fig. S2. Rejection of BP, TMP, and PFOA by TFC membrane after pre-compaction in the presence of these OMPs for 6 hours and 18 hours.

S3. Membrane characterization results

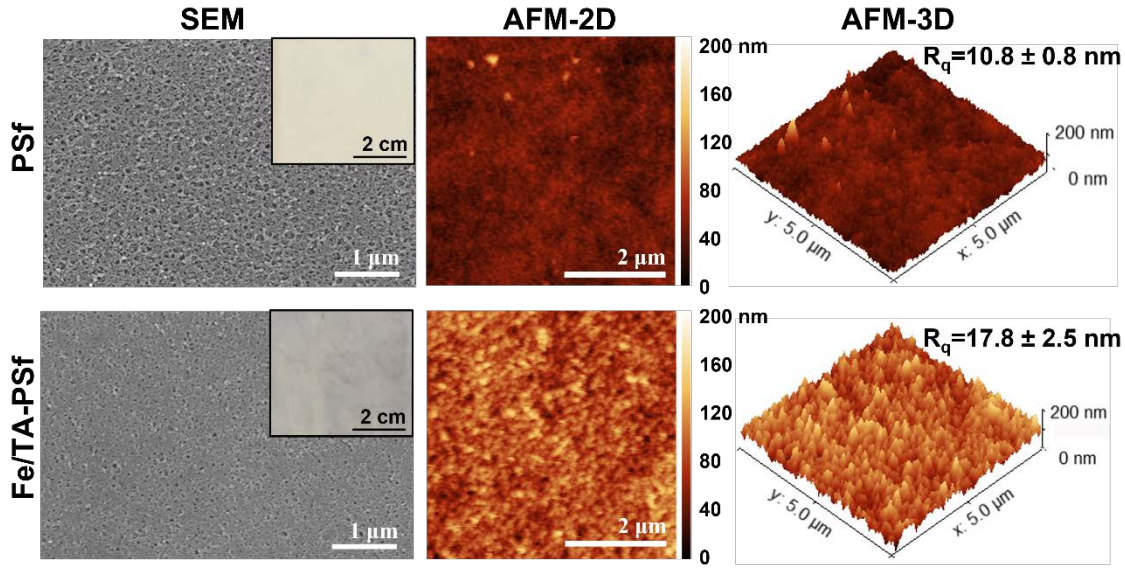

Fig. S3. SEM images, AFM-2D plane view, and AFM-3D view of the top surface for PSf and Fe/TA-PSf substrates. Inset are the digital photos of substrates. The roughness R_q value was the root mean square average of height deviations from the mean image data plane. Standard deviation was obtained from three independently scanned images.

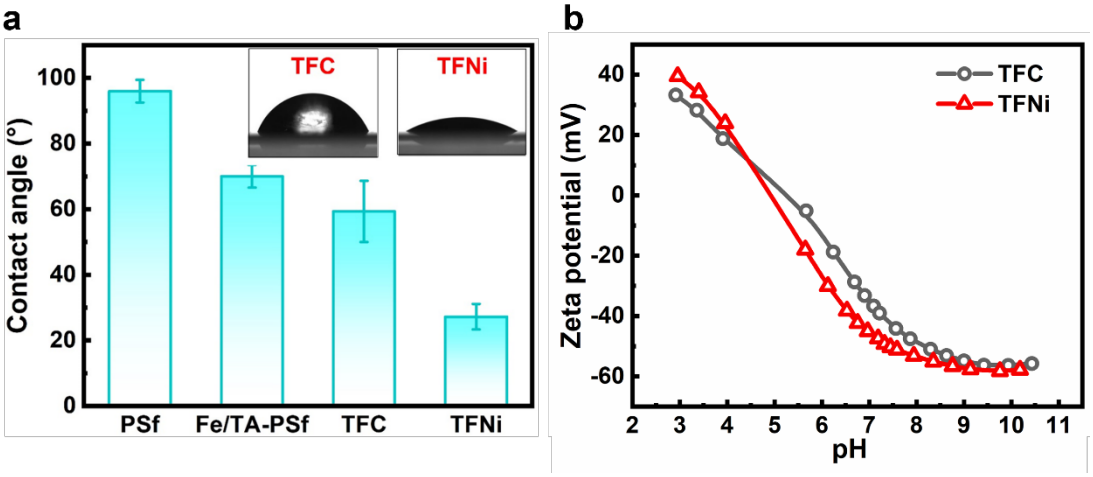

Fig. S4. (a) Water contact angle of substrates and NF membranes. Insets are the digital photos showing water contacting with NF membranes. Error bars were obtained from at least five measurements. (b) Surface zeta potential of TFC and TFNi membranes at pH from 3 to 10. The background electrolyte was 1 mM KCl. The solution temperature was kept at 25 ℃ and pH was adjusted by adding HCl or KOH.

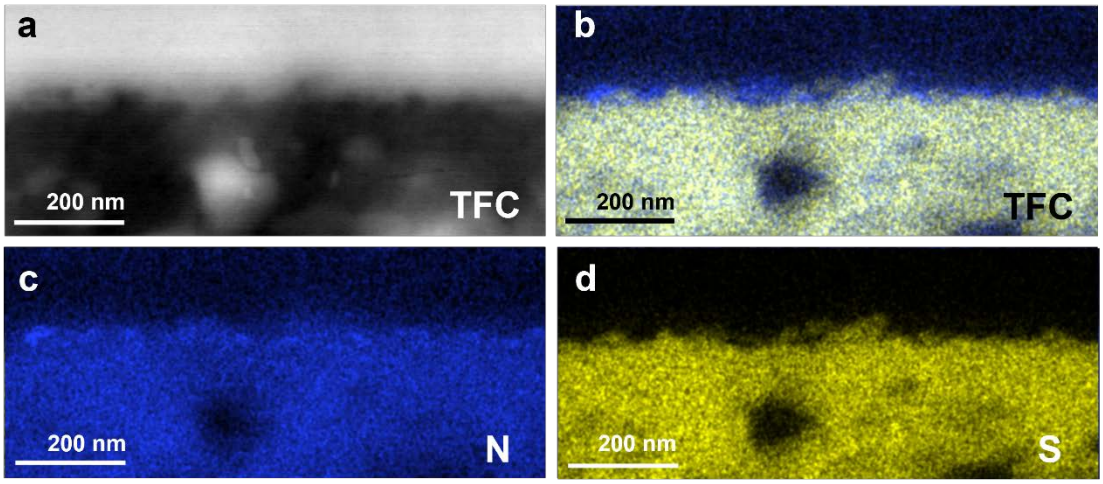

Fig. S5. (a) STEM cross-section image and (b) STEM-EDX elemental mapping of TFC membrane with (c) element nitrogen (N, blue) as an indicator for polyamide layer, and (d) sulfur (S, yellow) for polysulfone substrate.

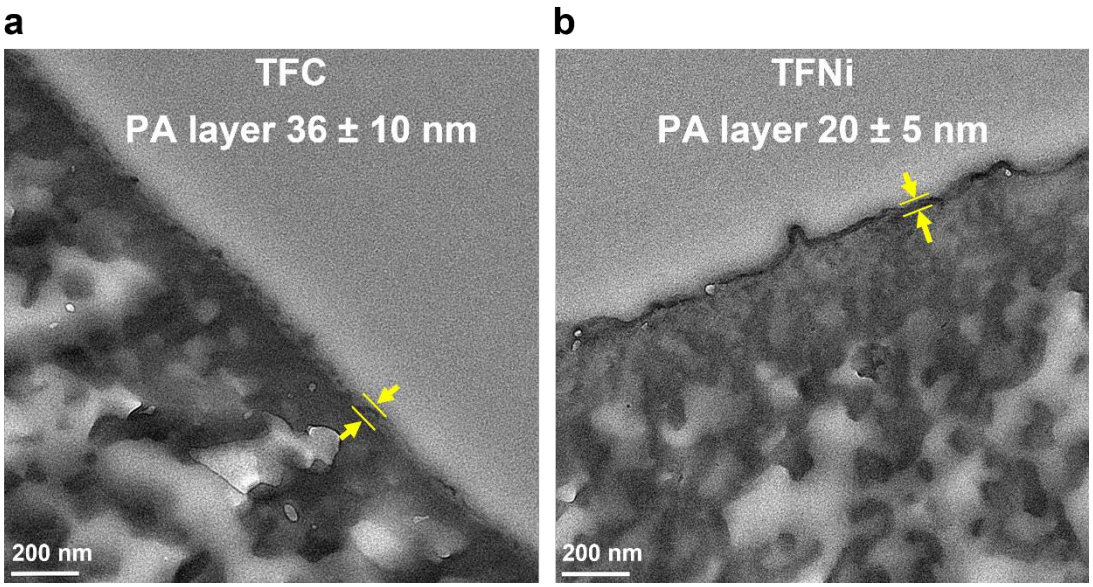

Fig. S6. STEM cross-section images of (a) TFC membrane and (b) TFNi membrane. Thickness of polyamide (PA) layer as denoted in yellow was measured by software Image J. At least ten different positions were measured for each sample.

Table S1

Different bonding states of C 1s in TFC and TFNi membranes.

Binding energy (eV)	~284.6	~286.0	~287.6
Peak assignment	C−C, C−H	C−O	O=C−O, O=C−N
TFC	75.4%	15.8%	8.8%
TFNi	66.7%	17.9%	15.4%

S4. Estimation of enhancement of water permeance

Water flux J_v of NF membrane can be simply modeled by using Hagen-Poiseuille equation (Wang and Lin, 2021):

$$J_V = \frac{r_p^2(\Delta p - \Delta\pi)}{8\eta L_e} \quad \text{(S1)}$$

where r_p is the membrane mean pore size, Δp is the hydraulic pressure applied, $\Delta\pi$ is the osmotic pressure difference across membrane, η is the dynamic viscosity of water, L_e is the effective membrane thickness defined by tortuosity τ, porosity ε, and thickness L via **Eq. S2**:

$$L_e = \frac{\tau L}{\varepsilon} \quad \text{(S2)}$$

To take into account the influence of surface roughness on the measured water permeance A, we further multiply J_v by membrane surface roughness ratio S:

$$A = \frac{J_V}{\Delta p - \Delta\pi} \times s = \frac{r_p^2 S}{8\eta L_e} \quad \text{(S3)}$$

where S is the ratio of membrane surface area over projected area obtained from AFM result.

Based on characterization result (**Table S2**), the water permeance of TFNi membrane is estimated to be **1.13** times of TFC membrane, which is much lower than the experimental result of A_{TFNi}/A_{TFC} (**2.54**).

It is important to note that the simple model presented above assumes water passes through the polyamide layer in the normal direction, such that the transport distance is governed by the thickness of the polyamide layer. In reality, the polyamide layer in a TFC membrane is supported by a substrate with certain porosity, which imposes a critical geometrical constraint – water has to reach to the pores of the substrate after passing through the polyamide layer. This geometrical constraint results in greatly

increased transport distance compared to the thickness of the polyamide layer (see schematic illustration in **Table 3**), leading to major reduction in the available water permeance (Long et al., 2022). Nevertheless, including a highly permeable interlayer or nanovoids in the membrane can mitigate this inefficiency, as it allows water to pass through the polyamide layer in the near-normal direction within the high-resistance layer and then to transport in the lateral direction via the low-resistance interlayer or nanovoids (**Table 3**) – a phenomenon known as the gutter effect (Wang et al., 2022). In the current study, the major difference between the enhancement factor predicted based on **Eq. S3** and the experimental value (1.13 vs. 2.54) can be attributed to optimized water transport pathways due to the gutter effect, which is consistent with existing modeling (Hu et al., 2023; Wang et al., 2022) and experimental studies (Long et al., 2022; Yang et al., 2020).

Table S2

Parameters used to estimate enhancement of water permeance.

	r_p (nm)	S	L (nm)	τ	ε
TFC	0.79	1.06	36	Not measured, assumed to be the same.	Not measured, assumed to be the same.
TFNi	0.61	1.12	20		

S5. Membrane separation performance

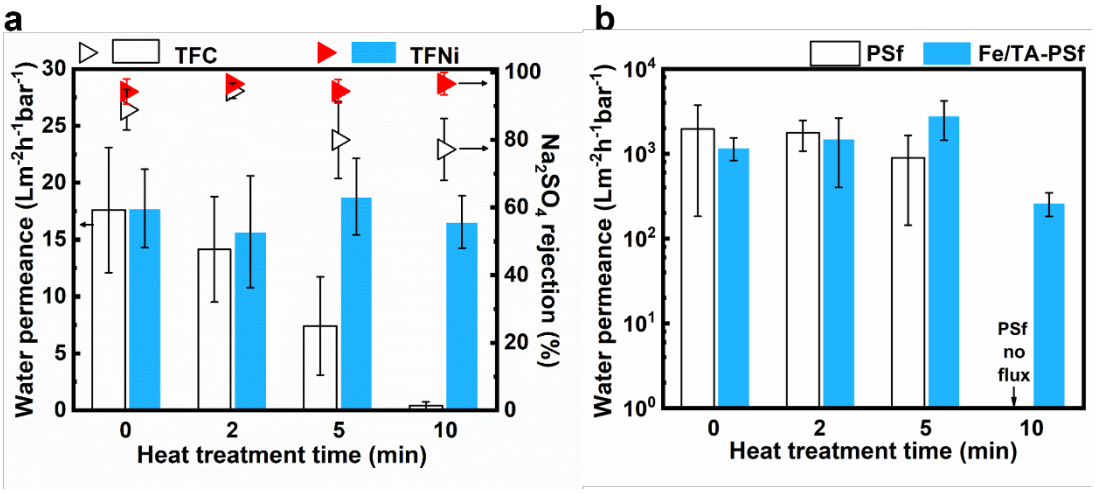

Fig. S7. Effects of heat treatment time on (a) membrane water permeance and Na_2SO_4 rejection and (b) substrate water permeance. NF membranes received different heat treatment time in 60 ℃ oven immediately after IP reaction. Bare substrates without conducting IP reaction were also put into 60 ℃ oven for different curing time. Testing conditions are as follows: 1000 mg/L Na_2SO_4, 25 ℃, pH 6.5~7.5, crossflow velocity 16.7 cm/s, 5 bar pre-compaction for two hours before testing NF membrane separation performance. Pure water, 25 ℃, pH 6.5~7.5, crossflow velocity 16.7 cm/s, 3 bar pre-compaction for 30 min before testing substrate water permeance. Error bars were obtained from at least three measurements.

It is worthwhile to note that the PSf substrate became significantly less permeable to water after 10 min heat treatment. Since the heat treatment process has been widely adopted by membrane manufacturers, in this study we chose to heat-cure the membranes for five minutes after IP reaction to make the fabrication method comparable with practical situation.

S6. Estimation of membrane pore size

To determine the membrane pore size distribution, firstly we plotted neutral solute rejection data (R_t) against their Stokes radii (**Table 1**). Assuming the pore size follows log-normal distribution (Liang et al., 2020; Van der Bruggen and Vandecasteele, 2002; Youm and Kim, 1991), we used the "log-normal cdf" function (**Eq. S4**) to non-linear fit the scattered points in Origin Software. From the fitted statistics, we picked out the radius r_1 when the rejection is equal to 50% and r_2 corresponding to rejection of 84.13%. Let the mean solute radius ($\overline{r}_s$) equal to r_1 and deviation (σ) equal to ($\ln r_1 - \ln r_2$). Then, we calculated mean pore radius ($\overline{r}_d$) by using $\overline{r}_p = \frac{1}{0.416}\overline{r}_s$ which is obtained from modified Ferry's model (**Eq. S5**) that considers the size exclusion effects and friction hindrance (Werber et al., 2016; Yang et al., 2017). Taking the $\overline{r}_p$ and σ value into **Eq. S6**, finally we got the probability density function curve of pore size distribution as shown in **Fig.4**.

$$R_t = \frac{1}{\sqrt{2\pi}}\int_{-\infty}^{y} e^{-u^2/2}du \tag{S4}$$

where

$$y = \frac{\ln r_s - \ln \overline{r}_s}{\sigma}$$

$$R_t = 1 - \{1 - [\lambda(\lambda - 2)]^2\}\exp(-0.7146\lambda^2) \tag{S5}$$

where

$$\lambda = \frac{r_s}{r_p}$$

When $R_t = 50\%, \lambda = 0.416$

$$\overline{r}_p = \frac{1}{0.416}\overline{r}_s$$

$$\frac{dF(r_p)}{dr_p} = \frac{1}{r_p\sigma\sqrt{2\pi}}\exp\left[-\frac{(\ln r_p - \ln \overline{r}_p)^2}{2\sigma^2}\right] \tag{S6}$$

S7. OMPs rejection by membranes with different heat treatment duration

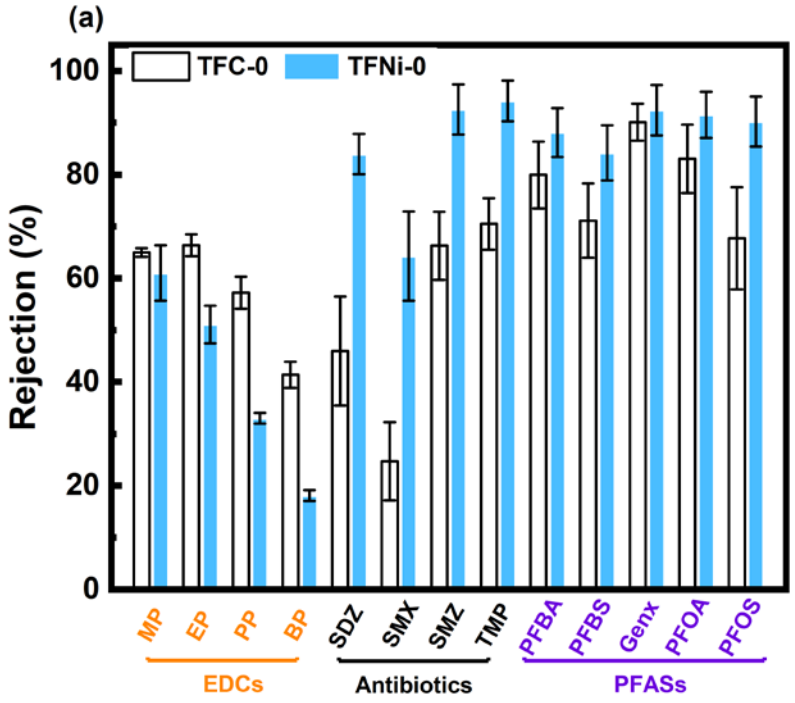

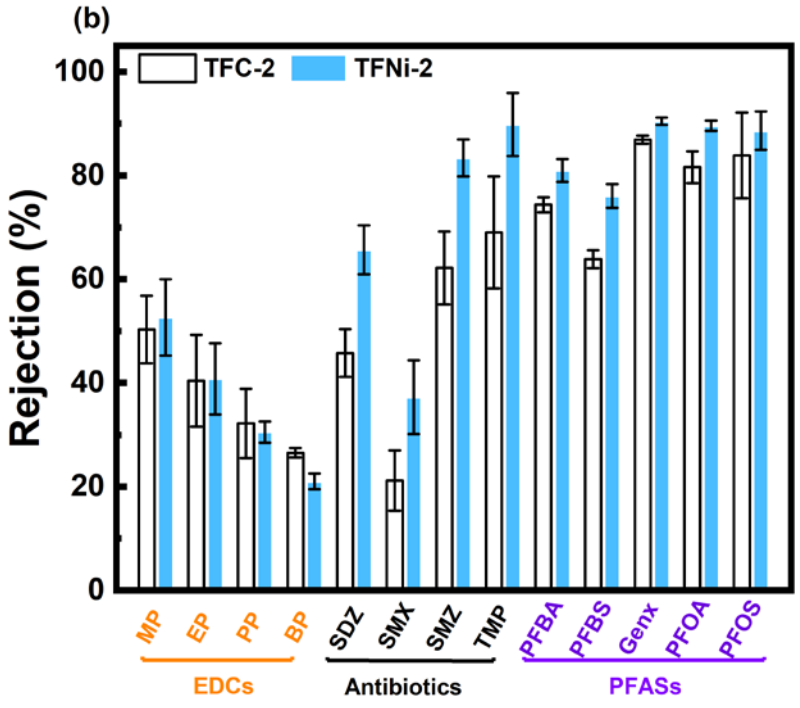

Fig. S8. Rejection of OMPs by TFC and TFNi membranes (a) without heat treatment and (b) with 2 min heat curing time. Error bar was obtained from at least three independent measurements.

S8. Sorption of OMPs onto NF membranes

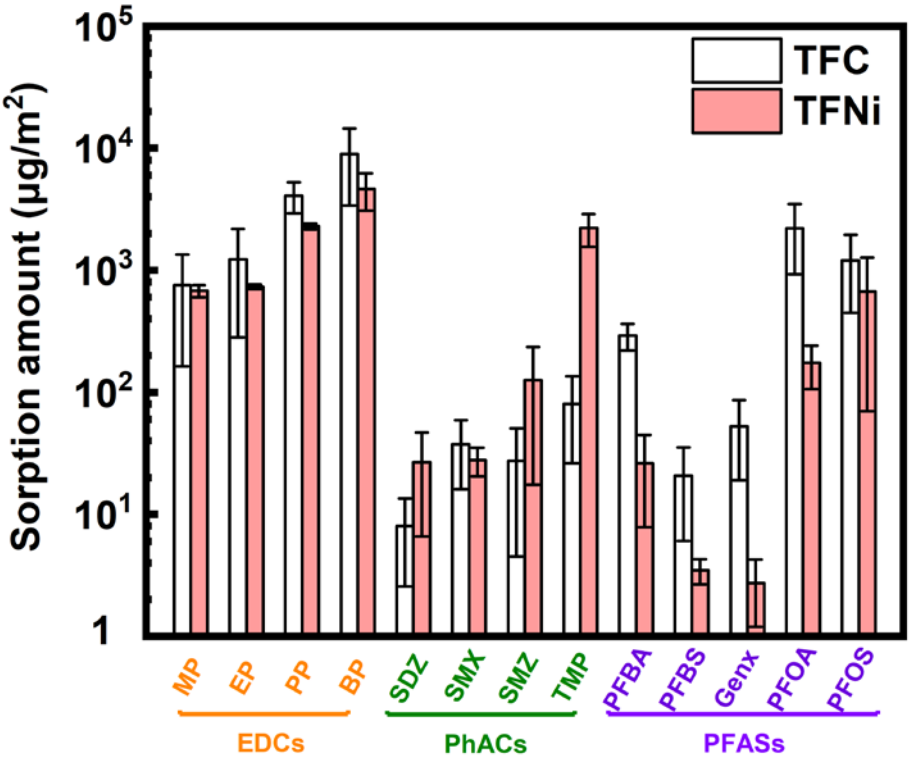

Fig. S9. Sorption amount of EDCs, PhACs, and PFASs onto TFC and TFNi membranes.

To determine the sorption amount of OMPs onto membranes, the membranes were taken out of cells after filtration test, soaked in 20 ml methanol, and shaken at 50 rpm for 24 hours. These extractions were then diluted with Milli-Q water to make a working solution of methanol:H_2O=1:4 for the analysis of PFBA, and methanol:H_2O=1:1 for other OMPs. Samples were analyzed by LC-MS/MS and the standard curve ranged from 0.1–500 μg/L. Error bars were obtained from three independent measurements.

S9. Passage and sorption of EDCs by TFC and TFNi membranes

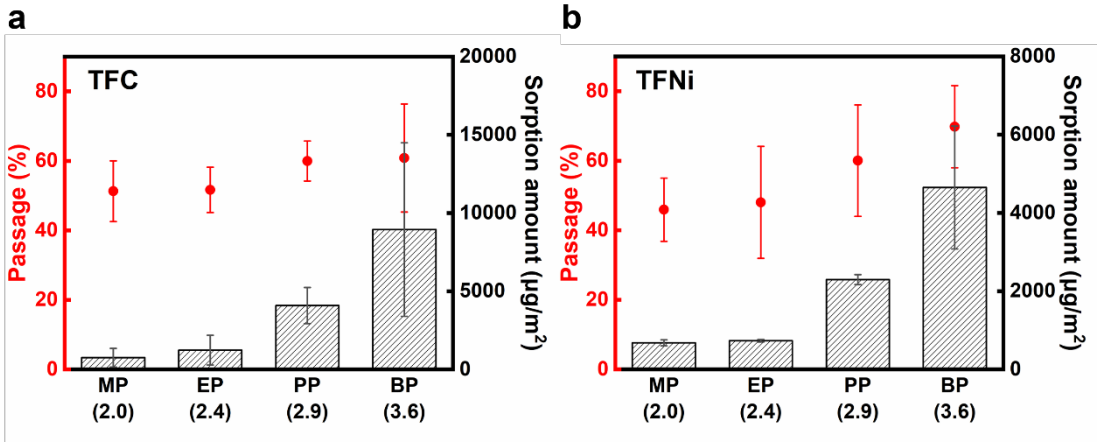

Fig. S10. EDCs passage and sorption amount by (a) TFC membranes and (b) TFNi membranes. The four EDCs are listed following the order of molecular weight MP<EP<PP<BP with log K_{ow} value annotated in bracket. Error bars were obtained from three independent measurements.

Passage and sorption amount of EDCs seem to increase with hydrophobicity even though the molecular size increase at the same time, indicating the hydrophobic interaction surpasses the size exclusion effects.

S10. OMPs selectivity of an Fe/TA layer

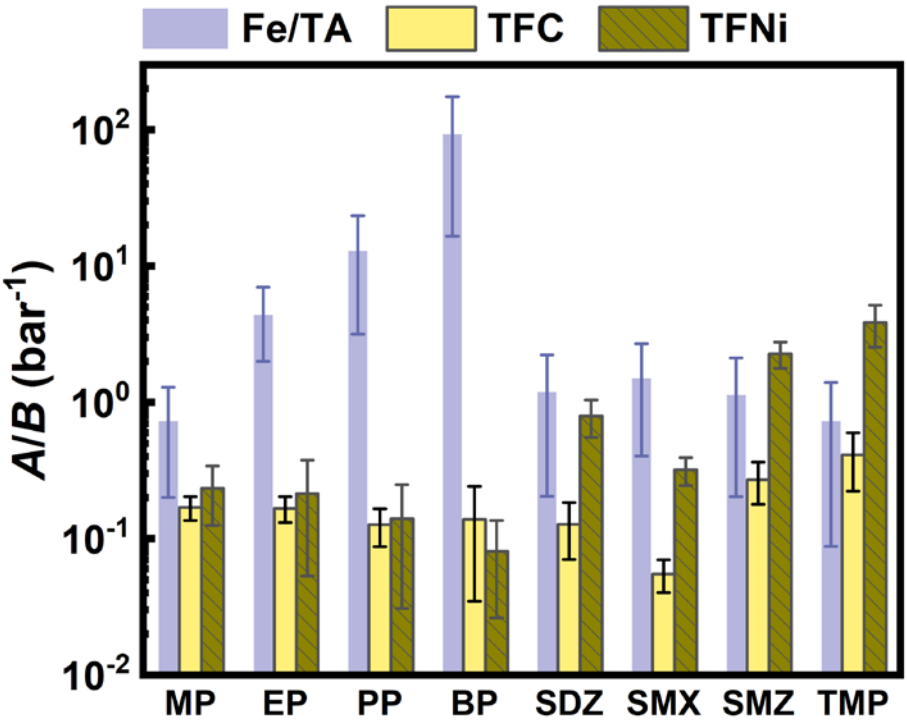

Fig. S11. Water-solute selectivity (*A*/*B*) of EDCs and PhACs by substrate coated with Fe/TA layer, TFC membrane, and TFNi membrane. Selectivity of the Fe/TA layer was obtained from our previous work (Guo et al., 2019).

References

Guo, H., Peng, L.E., Yao, Z., Yang, Z., Ma, X., Tang, C.Y., 2019. Non-polyamide based nanofiltration membranes using green metal–organic coordination complexes: implications for the removal of trace organic contaminants. Environ. Sci. Technol. 53 (5), 2688-2694.

Hu, Y., Wang, F., Yang, Z., Tang, C.Y., 2023. Modeling nanovoid-enhanced water permeance of thin film composite membranes. J. Membr. Sci., 121555.

Liang, Y., Zhu, Y., Liu, C., Lee, K.-R., Hung, W.-S., Wang, Z., Li, Y., Elimelech, M., Jin, J., Lin, S., 2020. Polyamide nanofiltration membrane with highly uniform sub-nanometre pores for sub-1 Å precision separation. Nat. Commun. 11 (1), 2015.

Long, L., Wu, C., Yang, Z., Tang, C.Y., 2022. Carbon Nanotube Interlayer Enhances Water Permeance and Antifouling Performance of Nanofiltration Membranes: Mechanisms and Experimental Evidence. Environ. Sci. Technol. 56 (4), 2656-2664.

Van der Bruggen, B., Vandecasteele, C., 2002. Modelling of the retention of uncharged molecules with nanofiltration. Water Res. 36 (5), 1360-1368.

Wang, F., Yang, Z., Tang, C.Y., 2022. Modeling Water Transport in Interlayered Thin-Film Nanocomposite Membranes: Gutter Effect vs Funnel Effect. ACS ES&T Eng. 2 (11), 2023-2033.

Wang, R., Lin, S., 2021. Pore model for nanofiltration: History, theoretical framework, key predictions, limitations, and prospects. J. Membr. Sci. 620, 118809.

Werber, J.R., Osuji, C.O., Elimelech, M., 2016. Materials for next-generation desalination and water purification membranes. Nat. Rev. Mater. 1 (5), 1-15.

Yang, L., She, Q., Wan, M.P., Wang, R., Chang, V.W.-C., Tang, C.Y., 2017. Removal of haloacetic acids from swimming pool water by reverse osmosis and nanofiltration. Water Res. 116, 116-125.

Yang, Z., Wang, F., Guo, H., Peng, L.E., Ma, X.-h., Song, X.-x., Wang, Z., Tang, C.Y., 2020. Mechanistic insights into the role of polydopamine interlayer toward improved separation performance of polyamide nanofiltration membranes. Environ. Sci. Technol. 54 (18), 11611-11621.

Youm, K.H., Kim, W.S., 1991. Prediction of intrinsic pore properties of ultrafiltration membrane by solute rejection curves: effects of operating conditions on pore properties. J. Chem. Eng. Jpn. 24 (1), 1-7.